



1 Controls of the Latitudinal Migration of the Brazil-Malvinas

² Confluence described in MOM6-SWA14

- 3 Nicole Cristine Laureanti^{1,2,3}, Enrique Curchitser¹, Katherine Hedstrom⁴, Alistair Adcroft⁵, Robert
- 4 Hallberg⁶, Matthew J. Harrison⁶, Raphael Dussin⁷, Sin Chan Chou³, Paulo Nobre³, Emanuel Giarolla³
- 5 and Rosio Camayo³
- 6 ¹Department of Environmental Sciences, Rutgers, The State University of New Jersey, New Brunswick, NJ, USA
- 7 ²Potsdam Institute for Climate Impact Research, Potsdam, BB, Germany.
- 8 ³National Institute for Space Research (INPE), Cachoeira Paulista, SP, Brazil
- 9 ⁴College of Fisheries and Ocean Sciences, University of Alaska Fairbanks, Fairbanks, AK, USA
- 10 ⁵Princeton University, Princeton, NJ, USA
- 11 ⁶NOAA/OAR/Geophysical Fluid Dynamics Laboratory, Princeton, NJ, USA
- 12 ⁷UCAR, Boulder, CO, USA
- **13** *Correspondence to*: Nicole C. Laureanti (nicole.laureanti@pik-postdam.de)
- 14 Abstract. The distribution and productivity of nutrients, eddy formation, energy dissipation, and other ocean properties are
- 15 influenced by the variability of Western Boundary Currents (WBCs). In the Southwestern Atlantic, the key features are the
- 16 Brazil-Malvinas Confluence (BMC) and the North of Brazil Current (NBC). This work investigates them using a 20-year
- 17 high-resolution ocean model simulation with the Modular Ocean Model version 6 (MOM6) 1/14° configuration of the
- 18 Southwestern Atlantic (SWA). The results reveal a significant deviation in the path and trends of volume transport of the
- 19 WBCs over the decades. The Brazil-Malvinas Confluence (BMC) region gets saltier and warmer, with increased kinetic
- 20 energy and transport. Although transport trends in the NBC indicate reduced transport, this results from weaker wind forcing,
- 21 which reduces the mixing layer depth in the simulation and the subsurface transport in the region. The warming in the Brazil
- 22 Current region triggers a stronger southward flow, resulting in a southward shift of $0.93^{\circ} \pm 0.08$ of latitude/decade in the
- 23 BMC separation. Working against this flow, the propagation of the Kelvin Waves from the Eastern Pacific Ocean induces a
- 24 northern shift of the BMC, revealed by topographic Kelvin waves in the spectral analysis. This Pacific-Atlantic inter-basin
- 25 relation indicated here underscores the importance of propagating Pacific disturbances into the region to maintain the
- **26** positioning of the BMC and its properties under a warming Atlantic Ocean.
- 27 Keywords: Western Boundary Currents; Brazil-Malvinas; climate trends; Kelvin topographic waves

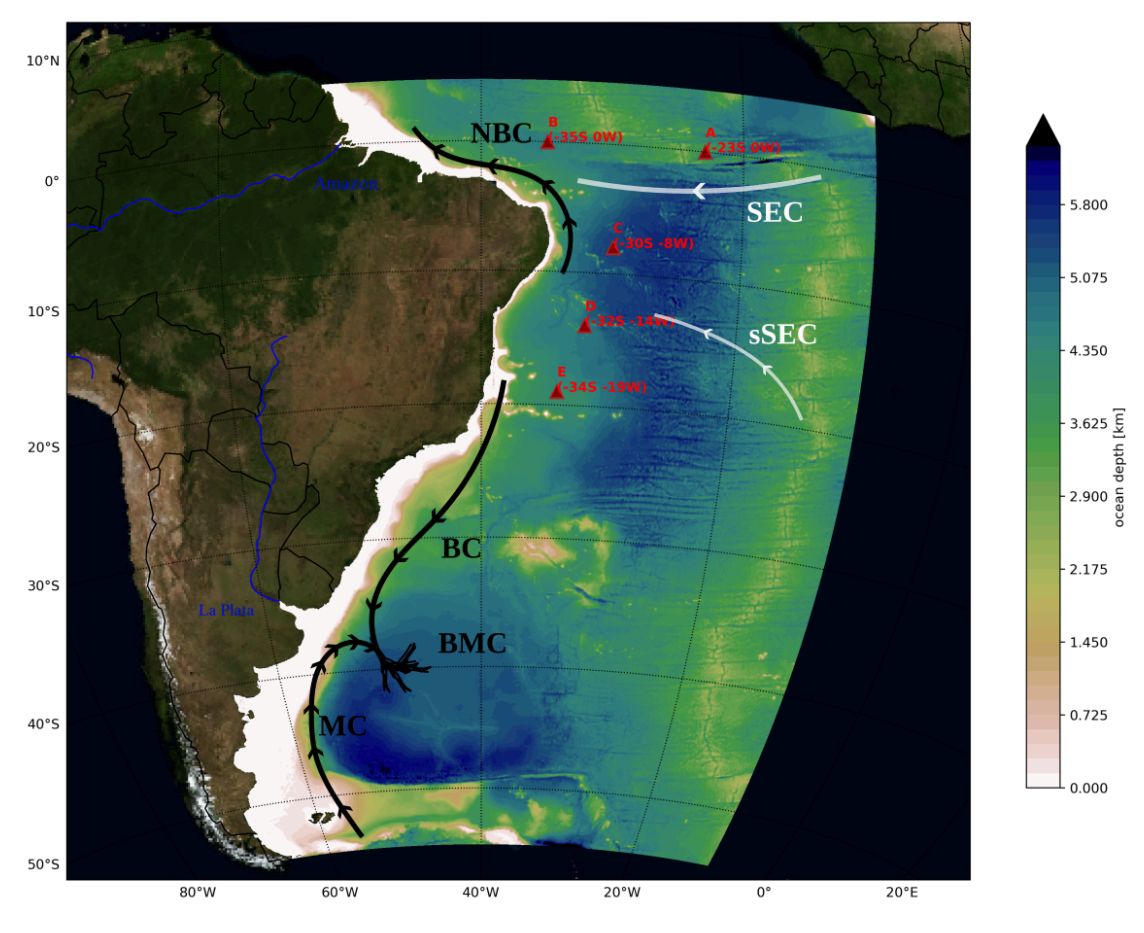




28 1 Introduction

35

Recent studies have revealed a relationship between the Southwestern Atlantic Ocean and extreme precipitation events in South America (Rodrigues et al., 2019; Pezzi et al., 2022; Laureanti et al., 2024). The investigation of this ocean circulation was also motivated by oil spills and other accidents polluting the Brazilian coastline, striking important naturally preserved areas (Nobre et al., 2022). Climate studies in the region have focused on heat budgets and trends (Muller et al., 2021; Franco et al., 2020). Improving the circulation description in this region can result in a better understanding of the dynamics, including even that of the CO2 distribution (Valerio et al., 2021; Bonou et al., 2016).



36 Figure 1: The Southwestern Atlantic simulation domain. The arrows illustrate near-surface currents: from north to south, the 37 South Equatorial Current (SEC) and its southern branch (sSEC), the North Brazil Current (NBC), the Brazil Current (BC), the 38 Malvinas Current (MC) and the Brazil-Malvinas Confluence (BMC). The Western Boundary Currents (WBCs) are in black. The 39 shaded colors indicate the topography in the Southwestern Atlantic Ocean used in MOM6 simulations. The locations of the 540 PIRATA buoys with observational data are in red. The locations of the major rivers in this domain are shown in blue. Satellite 41 images from Blue Marble: Next Generation define the terrain contours by NASA Earth Observatory.

42 The Atlantic Ocean is an energetic region with both surface and undercurrents between the Brazilian eastern coast and the 43 African western coast. Figure 1 illustrates the sea surface currents in this region, including the North Brazil Current (NBC)





44 and the Brazil Current (BC), whose flow is maintained by the southern branch of the South Equatorial Current (sSEC). The 45 sSEC redirects toward South America after originating in the Angola Gyre off the Western African Coast. The BC is 46 intercepted by the Malvinas Current (MC) as it flows southward, forming the Brazil-Malvinas Confluence (BMC). This 47 region experiences intense oceanic mesoscale activity due to the retroflection of these currents (Oliveira et al., 2009). The 48 MC originates in higher latitudes and flows northward, driven by the Antarctic Circumpolar Current (ACC). Meanwhile, the 49 NBC encounters the continental shelf in Northwestern Brazil, where its retroflection generates eddy propagation (Bueno et 50 al., 2022; Garzoli et al., 2004). The Western Boundary Currents (WBCs) mainly follow the coastline, comprising unique 51 dynamic properties and interactions with the continental shelf, a common characteristic in the BC, MC, and NBC.

52

53 The wind plays a dominant role in the variability of the WBCs (Wunsch and Ferrari, 2004). It impacts the mesoscale 54 structure within the Gulf Stream, which is a WBC in the Northwestern Atlantic Ocean, affecting the Mean Kinetic Energy 55 (MKE) to Eddy Kinetic Energy (EKE) conversions along the coast (Kang et al., 2016). The wind contribution to the BMC 56 variability can be explained by the frequent passage of atmospheric fronts at those latitudes that alter the predominant wind 57 direction and cause sudden reversal of the currents throughout the water column (Campos et al., 2013; Lago et al., 2019). 58 Furthermore, specific analysis of the MC near the Patagonian shelf has demonstrated its modulation by wind stress (Guerrero 59 et al., 2014; Palma et al., 2004; Lago et al., 2019). Additionally, winds also influence the Plata River discharge impacting the 60 BC flow (Piola et al., 2005; Campos et al., 2013). Northwesterly wind-stress anomalies commonly induce heavy runoff over 61 summer, spreading river plumes meridionally. During wintertime, strong southwesterly winds intensify a northward current, 62 causing freshwater discharges from the La Plata Basin to move northward. The seasonality of the atmospheric patterns also 63 contributes to precipitation inputs, which has been considered a contributor to ocean variability (Campos et al., 2013; Lago et 64 al., 2019; Palma et al., 2004). An interannual variability influence near the La Plata Basin is also evident, where the El 65 Niño-Southern Oscillation (ENSO) impacts freshwater discharges (Combes and Matano, 2018). In addition, some studies 66 have recognized the contribution of the South Atlantic Subtropical High (SASH) and the Intertropical Convergence Zone 67 (ITCZ) for the NBC variability. The SASH is the lower-level atmospheric dominant feature of the SEC, impacting the 68 SEC-NBC transport, while the ITCZ predominantly contributes to the Equatorial currents (Lumpkin and Garzoli, 2005; 69 Valerio et al., 2021). Important features related to its variability relate to the propagation of eddies in the NBC retroflection, 70 which results in a deviation of its natural path from 4°N to 8°N (Bueno et al., 2022; Valerio et al., 2021).

71

72 The highly energetic activity imposes challenges for diagnosing SST in places adjacent to WBC in General Circulation 73 Models (GCMs) (Stock et al., 2015; Adcroft et al., 2019). The oceanic grid resolution is key for simulating the physical 74 processes, as it determines the range of perturbations reproduced by the model (Adcroft et al., 2019; Hallberg, 2013; 75 Chassignet and Xu, 2021). At least a 1/8° resolution is required to explicitly capture the mesoscale baroclinicity in the 76 Southwestern Atlantic, while a resolution higher than 1/25° is recommended for continental shelf regions (Hallberg, 2013). 77 In addition, using a high-resolution ocean bathymetry induces better heat distribution by ocean currents (Griffies et al.,





78 2015). Regional numerical simulations can provide specific diagnostics, including distinct driving mechanisms for shelf 79 circulation. For instance, studies conducted by Palma et al. (2004, 2008) explored the significance of wind and tidal motion 80 in the Patagonian Shelf. The findings indicated that south of 40°S, circulation is primarily influenced by semidiurnal tidal 81 mixing (M2, S2, N2), wind, and the MC. The tidal mixing enhances bottom friction that balances the energy input by the 82 wind stress. Similar outcomes were described in a high-resolution simulation using the Regional Ocean Modelling System 83 (ROMS) (Combes and Matano, 2014a). Local winds contribute significantly to the shelf variability, but adding tides is 84 crucial to replicating the mixing near the coastal region accurately. The MC's transport is highly correlated with the 85 upwelling at the Patagonian shelf break and exhibits an out-of-phase relationship with the BC (Combes and Matano, 2014a).

87 There are also important WBCs relations driven by the proximity to the coastal slopes (Hughes et al., 2019). The internal 88 variability of the currents and transport in the WBCs offers a broader number of dynamic interactions, different from those in 89 the open ocean. Tropical waves from the Pacific follow the western South American coastline, propagate, and contribute to 90 the coastal dynamics in the Southwest Atlantic Ocean. Poli et al. (2022) reveal that Kelvin wave dispersion and Rossby wave 91 propagation from the Madden-Julian Oscillation are linked to the barotropic and baroclinic components of the coastal 92 trapped waves in the Southwest Atlantic Ocean.

93

86

94 This study aims to extend our understanding of this region by simulating and evaluating the ocean circulation. The relevance 95 of this implementation to global climate studies is the focus on the WBCs, indicating their unique variability and potential 96 drivers. Simulating the Southwestern Atlantic WBCs with a high-resolution framework allows for determining meaningful 97 characteristics of the variability of the mesoscale circulation.

98 This article is organized as follows: The first two Sections detail the model setup and the datasets. The results initially focus 99 on evaluating surface features and vertical structures by comparing them with local observational data in Section 3.1. The 100 analysis discusses the characteristics of the meso- and large-scale circulation within the domain, assessing the contribution of 101 winds and ocean transport to the overall dynamics in the model. Section 3.2 discusses the seasonal variability and trends of 102 the WBCs. In Section 3.3, we focus on the internal and external components of the variability of WBCs. The final section 103 contains the discussion and conclusions, offering an analysis of the variability of the WBCs circulation reproduced by the 104 model.

105 2 Model and Data

106 2.1 Model Description and Configuration

107 The model used in this work is the Modular Ocean Model version 6, developed by the Geophysical Fluid Dynamics 108 Laboratory (GFDL) from the National Oceanic and Atmospheric Administration (NOAA) (Adcroft et al., 2019). The model 109 was designed to represent the ocean's general circulation. The version used in this paper is capable of running on regional





110 configurations as a result of the implementation of open boundary conditions. The horizontal grid extends from longitude 111 69°W to 9° W and from latitude 55°S to 5°N, at 1/14° resolution (approx. 7 km). The model domain uses the topography 112 displayed in Figure 1. The ocean bathymetry was interpolated from a horizontal resolution of 450 meters from the General 113 Bathymetric Chart of the Oceans (GEBCO) (Giribabu et al., 2023). The vertical discretization distributes 75 levels from 3 114 meters up to 6,500 meters of depth, varying in thickness from 2 m near the surface up to 250 m in the deep ocean. The 115 model uses the z* vertical coordinate, which is a height-based coordinate rescaled with the free surface (Adcroft and 116 Campin, 2004). Under this setup, the model simulation started on 1st January 1997 and ended on 31st December 2016, a 117 total of 20 years.

118

119 The model uses initial and boundary conditions data from GLORYS 12v1 ocean reanalysis, developed by the Copernicus 120 Marine Environment Monitoring Service (CMEMS), with a daily frequency and an 8-km resolution (1/12°) (Jean-Michel et 121 al., 2021). The atmospheric forcing is the hourly reanalysis data from the European Centre for Medium-Range Weather 122 Forecasts (ECMWF) fifth generation (ERA5) at 25 km (Hersbach et al., 2023). Ten tidal components from the global model 123 of ocean tides TPXO (Egbert and Erofeeva, 2002) are used in the boundaries and internal domain to force the barotropic 124 conditions through parametrization. The components are four semidiurnal (M2, S2, N2, and K2), four diurnal constituents 125 (K1, O1, P1, Q1), and two long-period constituents (Mm and Mf). The freshwater discharge is from the Global Flood 126 Awareness System (GloFAS) reanalysis dataset (Zsoter et al., 2021). To assimilate natural conditions, chlorophyll estimates 127 from the Sea-viewing Wide Field-of-view Sensor (SeaWiFS-NASA) (NASA, 2018) are inserted in the opacity scheme to 128 modify the estimate of the atmospheric radiation reaching the deepest layers. The MOM6 schemes are based on the physical 129 ocean model configuration of Ross et al. (2023). Parameterizations include the convection Energetic Planetary Boundary 130 Layer (ePBL) approximation (Reichl and Hallberg, 2018), the Fox-Kemper restratification for the mixing layer (Fox-Kemper 131 et al., 2011), while astronomical tides and the Kappa-shear scheme (Jackson et al., 2008) induces interior and bottom mixing, 132 respectively.

133 2.2 Data for Validation

The 20-year simulation is assessed by comparing mean fields with observational data. The World Ocean Atlas (WOA) temperature and salinity climatology (Locarnini et al., 2019; Zweng et al., 2019) and the Surface Mixed Layer Depth (MLD) climatology from de Boyer Montégut et al. (2004) correspond to the datasets of coarser resolution with a 1° resolution. A local comparison relates the model results to the observational data from 4 buoys from the Pilot Research moored Array in the Tropical Atlantic (PIRATA) project (Servain et al., 1998). The dataset consists of time series and vertical profiles of temperature and salinity over the tropical Atlantic, with five moored buoys in the tropical Atlantic, two on the equator that have data from January 1998 to recent years, and the other three are placed southern, with measurements starting in August 12005. The buoys are A: 0°S 23°W, B: 0°S 35°W, C: 8S° 30°W, D: 14°S 32°W, and E: 19°S 34°W and their locations are shown in Figure 1. The GLORYS12 v1 reanalysis, used as forcing and for comparison with model outputs, provides





143 comparable results in high-resolution daily data. Besides the assimilative schemes, this reanalysis uses ERA-Interim and 144 ERA5 data in the surface and the dynamical core from NEMO in 50 standard levels (Jean-Michel et al., 2021). The mean 145 winds from ERA5 are compared against the 0.125° QuickSCAT (QSCAT) satellite data, available between 1999 and 2009 146 (Hoffman and Leidner, 2005).

147 3 Results

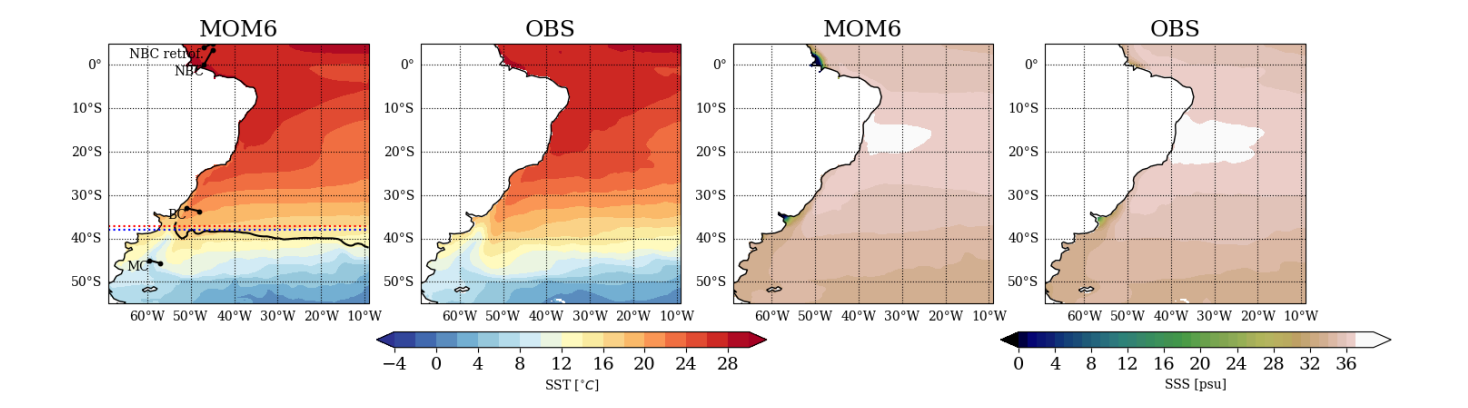
148 3.1 Evaluation of the Simulation Mean State

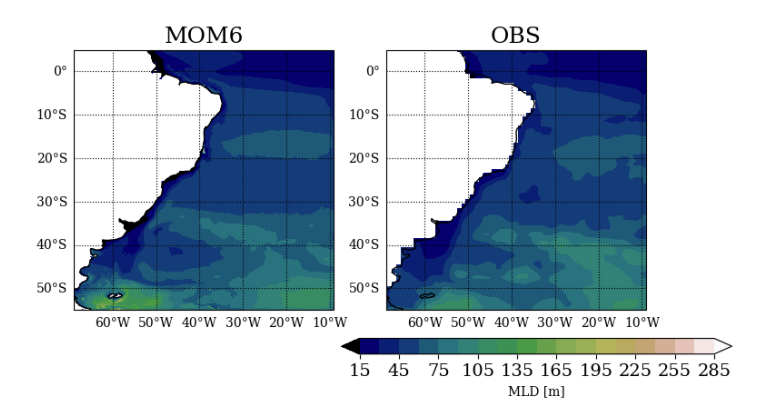
149 3.1.1 Ocean Surface

150 Surface variables often characterize the main features that develop in the ocean. Figure 2 displays the mean surface variables 151 from model outputs compared to observations. The fields originate from different horizontal resolutions, with a coarser 152 resolution for the observations, resulting in a lack of representation of higher-resolution structures, especially near the 153 coastline. Overall, the results indicate a good representation of the mean state fields. The central South Atlantic is the region 154 with the most similar SST patterns. The major differences appear in the open sea with colder SST in the eastern equatorial 155 Atlantic in the model. The difference in the BMC is negative and less than 1°C, which is more accurate than the one obtained 156 with the global 1/4° version of the model, with a positive bias greater than 2°C, using the same vertical model coordinate 157 (Adcroft et al., 2019), highlighting the benefits of increasing the horizontal resolution.









159 Figure 2: Sea Surface Temperature (top row), Salinity (middle row), and Mixed Layer Depth (bottom row), 20-year mean from the 160 simulation (left) and WOA observations (right). In (a), the illustrated black line is the 10°C isotherm at 200 m, where it meets with 161 the 1000 m isobath, an estimate proposed by Garzoli and Bianchi (1987) to indicate the BMC separation in the model. The dotted 162 curves represent the mean BMC separation using (red) GLORYS12s reanalysis and (blue) the obtained from satellite 163 observational sets by Goni et al. (2011).

164

165 The model captures the development of the BMC, with the location of the temperature gradients in the region. The 166 northward propagation of surface cold waters through the MC ends at approximately 37°S. The confluence with the BC 167 appears within this region, which is close to estimates from observational data (Figure 1; Goni et al., 2011; Lumpkin and 168 Garzoli, 2011). A similar gradient is found in the observations, but cooler temperatures emerge near the La Plata Basin coast. 169 The model shows extra fresher waters near the La Plata and the Amazon Basins, indicating that the salinity is close to zero 170 downstream of the basins. The model presents less salty waters than the observations at around 10-20°S, which appears to be 171 related to the river discharges. However, the freshwater inputs look trapped in shallower depths on the coastline, and 172 according to the ocean circulation (Figure 1), the fresher water inputs flow south for the La Plata River and northwest for the 173 Amazon River. The MLD pattern diagnosed by the ePBL's model scheme is consistent with the patterns of the observations 174 despite the impacts of the river on the coastline circulation.





175

176 Contrasting patterns between the shallow and deepest regions appear from comparing the model seasonal averages with 177 reanalysis from GLORYS12s with similar horizontal resolution (Jean-Michel et al., 2021). Figure 3 shows the sea surface 178 density for each trimester, estimated by the equation of state for ocean models considering temperature and salinity (Wright, 179 1997). There is a higher consistency in the seasonal density between the fields far from the coast. Some differences in 180 temperature contours emerge in the northwestern and southwestern South Atlantic, where the model keeps colder equatorial 181 waters during most seasons. Although the difference in the temperature field has maximum values of -1°C to the south of 182 30°S, especially during March to May (MAM) and June to August (JJA), it reproduces a weaker variance in the density field. 183 The difference in density in the tropics is unrelated to the temperature variations and indicates the presence of freshwater 184 inputs from the rivers, as indicated in Figure 2.

185

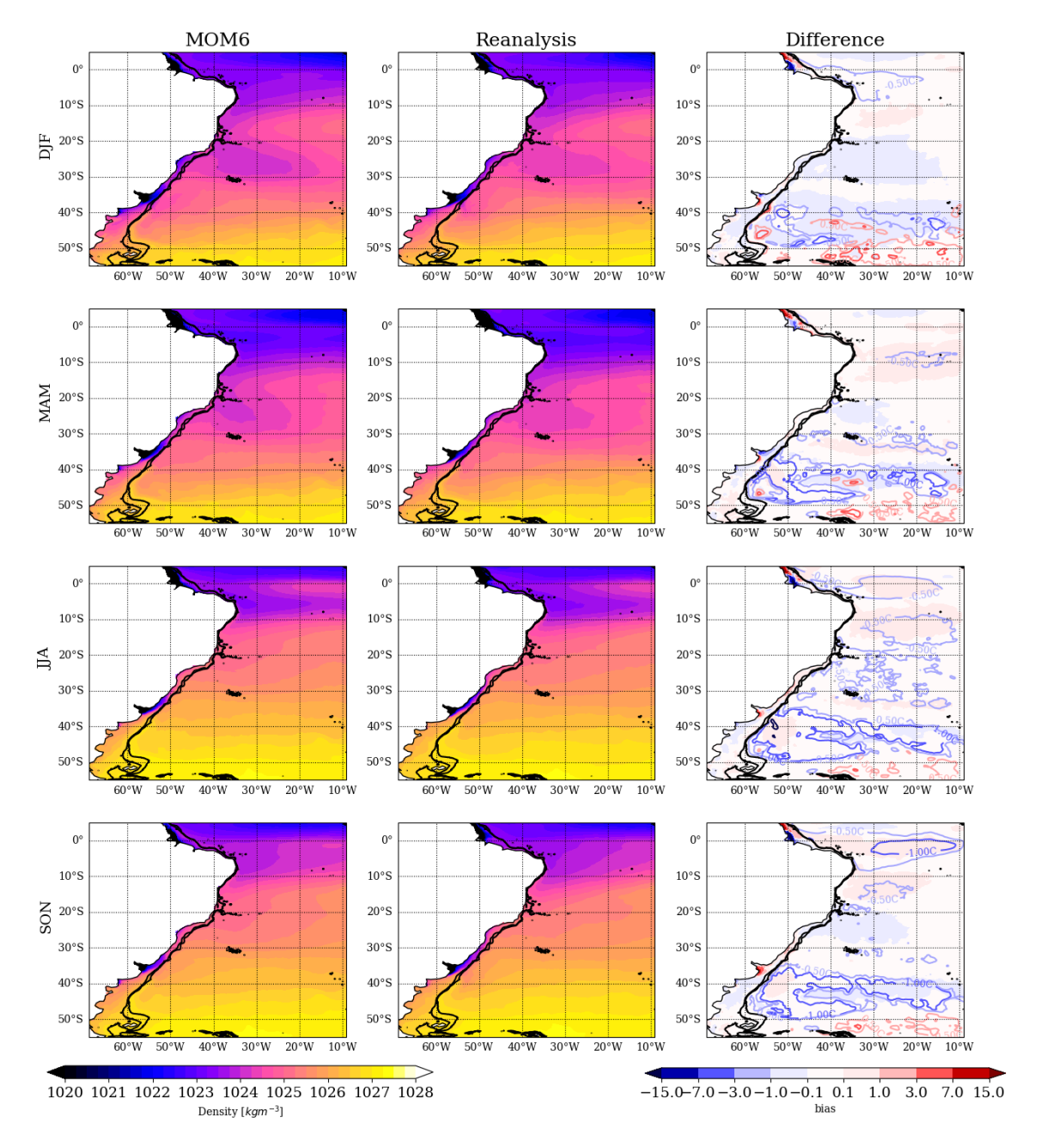
186 The most significant differences in density appear in the shallow areas in the Amazon region, which exhibits variability 187 related to the river's seasonality. The contrasting heavy rainfall related to the ITCZ displacement is related to the region's 188 variability (Valerio et al., 2021). It contributes significantly to the mean flow from December to February (DJF) until MAM, 189 with fewer discharges during JJA and September to November (SON). The difference in the density fields (Figure 3) 190 indicates that the model representation of the river discharges is more coherent during MAM, the period of higher freshwater 191 discharge. The model's salinity distribution is counterbalanced in the other drier seasons, showing reduced salinity in the 192 Amazon River basin and increased in the extreme northwest of the domain. Thus, deviations in the mixing of the river 193 discharges imply the appearance of a dipole of density northwest of the domain in Figure 3. The density is higher in the 194 model with more saline waters and lower in fresher waters.

195

196 Like the Amazon, the river seasonality implies modifications in the river discharges in the La Plata Basin. The model 197 overestimates the density downstream of the La Plata Basin due to more saline waters on the southwest coast, mostly during 198 SON. During winter (JJA), strong runoff during winter is enabled by the frequent passage of atmospheric systems when the 199 intense rainfall and wind spread the freshwater discharges of the river plume (Campos et al., 2013; Lago et al., 2019; Piola et 200 al., 2005).







203 Figure 3: Seasonal mean surface density for the MOM6 simulation, the reanalysis (GLORYS12) and error. Each row shows a 204 season, from the top to the bottom, DJF, MAM, JJA, and SON, marking the transition from austral summer to spring. The means 205 consider the period from 1997 until 2017. The contours in the right column show the temperature errors in the open ocean (depth $2006 \ge 1000$ m), with contours at ± 0.5 , 1.0, and 3.0° C. The thick black contours indicate the 200 and 1000 m isobaths.





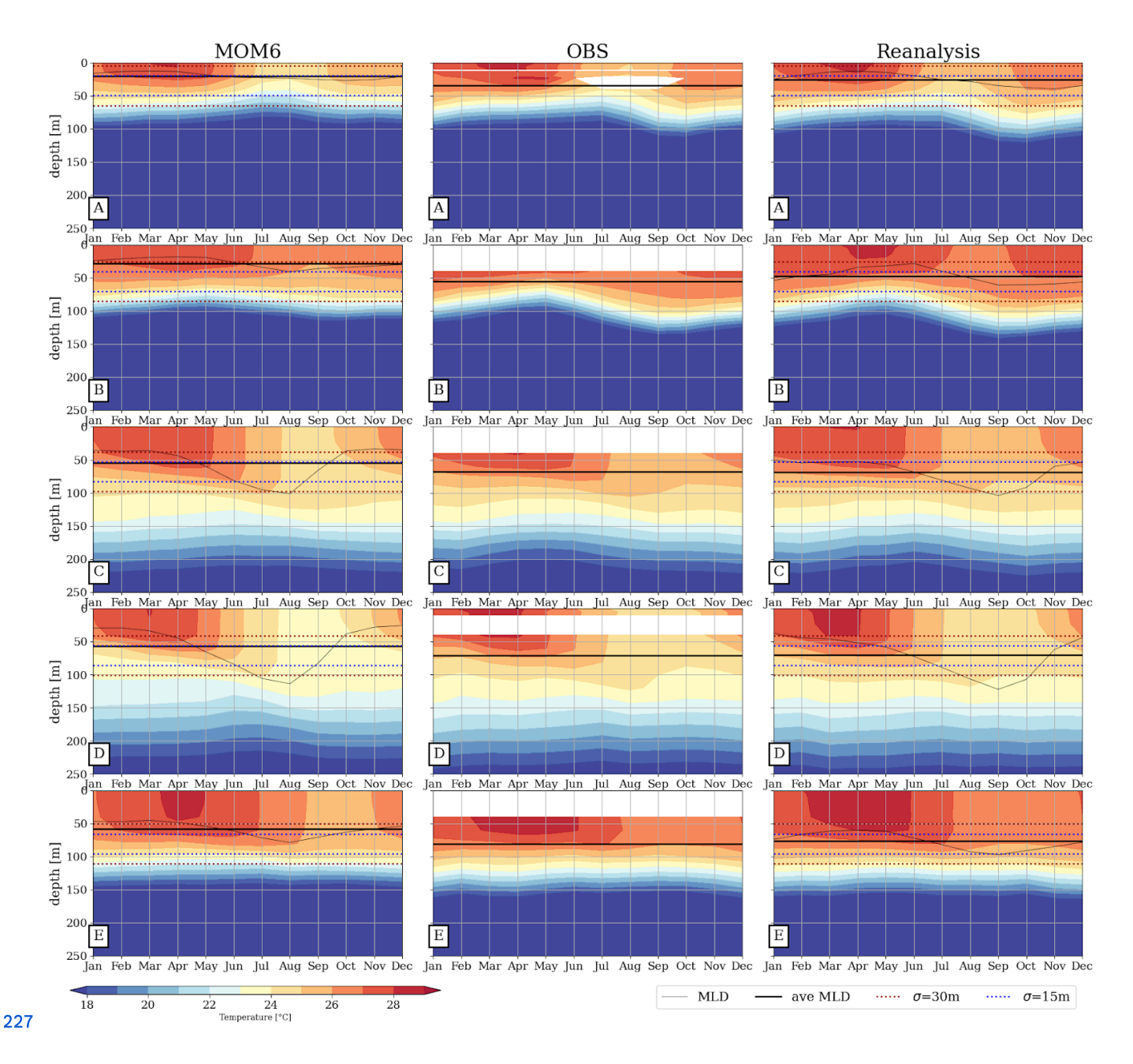
The importance of determining the advancement of freshwater plumes into the open ocean in both basins has been described in the literature (Valerio et al., 2021; Campos et al., 2013). Although the surface fields based on the 20-year model averages exhibited bias constrained by the coastline, the freshwater plumes accurately display the river seasonality. The river discharges simulated by the model represent the impact on the MLD seen in Figure 2. In addition, the salinity variations near the Amazon and La Plata basins also considerably impact the surface density comparable to the reanalysis (Figure 3). Although a similar resolution increases the consistency of the results in the basins, unbalanced freshwater amounts still occur. The results indicate that the amount of freshwater on the surface and the lower density contribute to less mixing in shallower depths. The similarity of the results far from the coast, especially MLD and density patterns, indicates that this unbalanced freshwater influence is primarily local at the delta of the Amazon and La Plata Rivers and does not lead to a 217 general bias.

218 3.1.2 Temperature Vertical Structure and Seasonal Variability

Temperature profiles in Figure 4 characterize the vertical structure in the ocean model against the reanalysis and the PIRATA buoys observations. The depth of the 18°C isotherm compared to the buoys evidences the conformity in the vertical structure. The 18°C isotherm in the A and B observations shows deeper seasonal fluctuations during SON, so the model fails in reproducing the structure. During the warmer season, MAM, when the warmer waters reach deeper layers in the observations, the model remains cooler until the wintertime. This effect reduces the MLD in the model, which shows a 30 m shallower MLD (Figure 4, right column) than the other datasets in the buoy sites (Figure 4, left and center). The difference is even more critical at the buoy B site, where the MLD is more than 30 m shallower in the model.





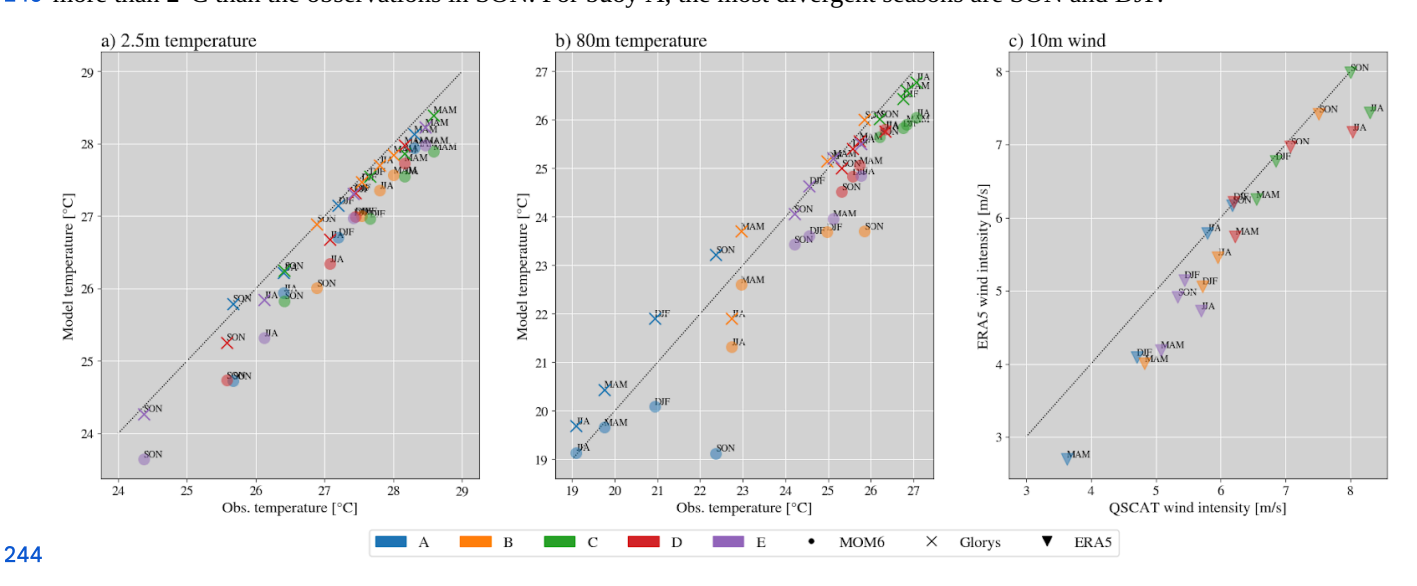


228 Figure 4: Mean annual cycle of the vertical profile of temperature and MLD at PIRATA buoy sites. The colors display the 229 temperature, and the lines are the MLD. The letters identify the buoy sites from A to E. MOM6 outputs are on the left column, 230 observed data from the PIRATA buoys are in the center, and reanalysis products are on the right. The MLD for observation and 231 reanalysis are estimated with the $\Delta T = 0.2^{\circ}$ C temperature threshold from a near-surface value and the 10 m. Missing data appears 232 at different depths in the observations and are shown in white. The dashed lines highlight depths above/below the mean 233 buoy-estimated MLD in blue with a difference of 15 m and in red 30 m.





235 The temperature at shallow and deeper regions shown at the buoy sites in Figure 5 explains the reduced heat entrainment 236 from the surface layers in the model. Near the surface, the model temperature is approximately $\leq 1^{\circ}$ C lower than the 237 reanalysis and the buoys through the seasons (Figures 3 and 5a). The model presents a well-defined seasonal cycle near the 238 surface (Figure 5a), with warmer temperatures during MAM and cooler in JJA and SON. More contrasting outliers are in the 239 80 m depth layer (Figure 5b). Compared to the model, the observations at sites A and B present 2°C warmer temperatures 240 during SON and 1°C warmer during DJF. In the other buoy sites (C, D, and E), far from the equatorial region (Figure 1), the 241 water column is deeper, and the model presents a reduced bias. The challenge of reproducing the 80 m temperature in the 242 equatorial region is observed even in the reanalysis (Figure 5b). This divergence for site B starts in JJA, getting colder by 243 more than 2°C than the observations in SON. For buoy A, the most divergent seasons are SON and DJF.



245 Figure 5: Seasonal 2.5-m and 80-m temperatures and 10-m winds, compared against observations. The graphs display the 246 temperature at 2.5 m (a) and 80 m (b) for the model and reanalysis compared to PIRATE buoy observations. In (c), the 247 atmospheric forcing for the model, 10-m wind from ERA5, compared to QSCAT satellite observation (Hoffman and Leidner, 248 2005). Colors distinguish the buoy sites from A to E. The model data is marked with circles, while the reanalysis from Glorys takes 249 crosses and ERA5 triangles. The seasons are named as DJF, MAM, JJA, and SON.

The tendency of the model to underestimate the entrainment of seasonal heat at the equator indicates a concern about the ITCZ displacement. The latitudinal ITCZ displacement causes the most intensive surface heating during MAM (Valerio et al., 2021), reproduced with lower bias by the model considering observations (Figures 3 and 5a). This enables the development of stratification and heating of the deeper layer in the following seasons. However, although the model reproduces the warmer temperatures during MAM and JJA, the deeper layers remain cooler until SON (Figure 5b). This deviation indicates that although the model receives the seasonal heat at the surface, it gets under-mixed during the stratified





257 period. In contrast, for the reanalysis to reproduce the heating and the accordant stratification structure during SON, the 80

258 m-depth waters are slightly warmer than the buoys for sites A and B.

259 The seasonal ITCZ displacement impacts wind speed in the buoy sites, which is a misleading diagnostic that can interfere

260 with ocean currents and mixing. The model wind forcing (ERA5) is compared to QSCAT satellite observations in Figure 5c

261 to observe this effect. Although the ITCZ depends most on the wind structure during DJF and MAM in the equatorial region,

262 ERA5 wind is slower than the observations through all seasons. During the warm season, buoy sites A, B, and E present

263 wind forcing almost 1 m/s slower. The wind pattern, which contributes to the vertical mixing, suggests that equatorial region

264 temperature biases occurs due to the lack of a wind-driven source.

265

266 The deviation of mixing in the adjacent layers and the freshwater discharges can be a response to the vertical coordinate

267 system. The heat uptake bias in the z-coordinate system is higher in comparison to the hybrid coordinate, as indicated in

268 (Adcroft et al., 2019). In addition, the weaker ERA5 10m-wind, compared to the estimates from satellite observations

269 (Figure 5c), leads to less mixing in the bottom layers since it dissipates the wind stress, the main energy source to the

270 currents, and subsequent horizontal transport. These weaker winds can also contribute to the salinity differences in the

271 northwestern part of the domain. Lighter density is placed in the Amazon Basin due to the weak zonal winds contributing to

272 constraining freshwater discharges to the surface. In turn, the lack of advection of freshwater results in salty and more dense

273 waters (> 7 kgm-3) in the northwest corner of the domain (Figure 3).

274 3.1.3 Meso- and Large-scale Circulation

275 The ocean circulation comprises the distribution of the current speeds and energy, potentially related to the tracer exchanges

276 in the domain. The analysis in this study allows the observation of meso and large-scale circulation as represented by the

277 model. The 20-year mean surface current speed model outputs in Figure 6a display the mean natural path of the main

278 currents, depicted in Figure 1: SEC, NBC, BC, and the MC, distinguished from the mean flow. The BC is observed through

279 the warm high-speed currents on the mid-western Atlantic flowing southward from 20°S. The MC surrounds the east of the

280 Patagonian Shelf on the Argentinean coast south of 40°S, and the eastward flow in 50°S marks the origin of the South

281 Atlantic Current. The mean speed field also allows the appearance of high-speed currents in the BMC, between 35°S and

282 45°S. In the northwest, the flow of the NBC and the connection with the SEC is also pronounced. The NBC is north of 5°N

283 and to the northwest. Thus, the model places the ocean currents that agree with the general location described by others

284 (Lumpkin and Garzoli, 2005; Oliveira et al., 2009).

285

286 The current speed standard deviation for the two main WBCs reveals that the model can reproduce the variability of these

287 features in various different shallow parts of the domain (Figure 6b and c). The NBC is the most prominent current in the

288 domain, and the speed reaching 1.5 m/s and the standard deviation of 0.45 m/s indicate larger variability. This dynamic

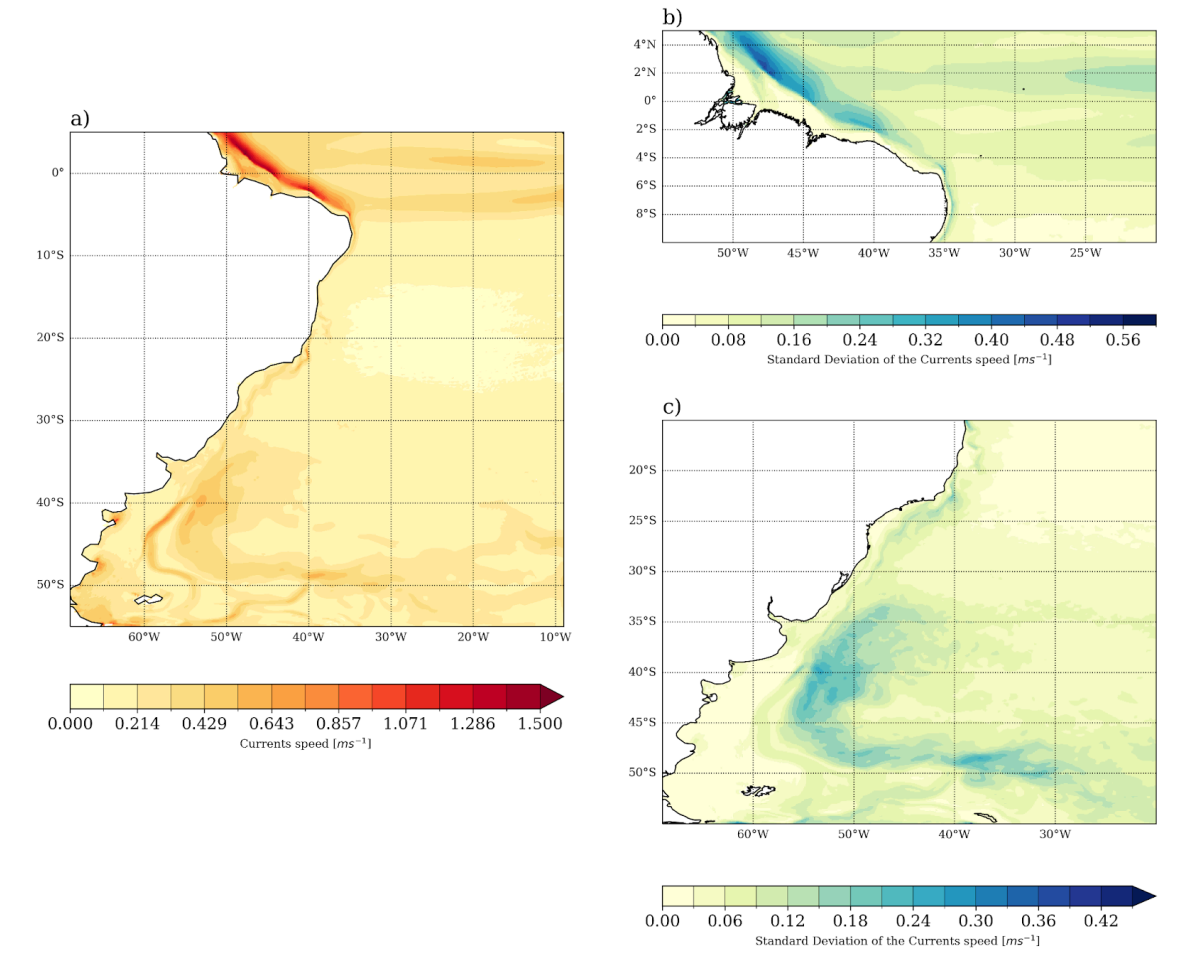
289 background induces the formation of mesoscale structures through the NBC retroflection (Bueno et al., 2022; Garzoli et al.,





290 2004). Part of this variability is due to the topographic gradient but also induced by the seasonal cycle and the river 291 discharges of the Amazon River. Another contributing factor is the SEC's high speed (> 0.45 m/s) and deviation (> 0.15 m/s) 292 in equatorial waters. The SEC maintains East-West oceanic transport, suffering from the seasonal effect drift due to the trade 293 winds, which decreases its intensity during DJF compared to JJA (Lumpkin and Garzoli, 2005). The propagation of 294 mesoscale eddies also induces the intense variability noted near the BMC. The high speed and deviation are constraints in an 295 area where the retroflection of the MC propagates eddies to the west. This region is known for the shelf-break upwelling, 296 where the significant depth gradient and the proximity to the MC contribute to the enhanced mixing and upwelling (Figure 297 1).

298



300 Figure 6: Mean sea surface currents (m/s) (a) and standard deviation of the mean speed (m/s) for the NBC (b) and the BMC (c) 301 regions. The standard deviation considers the monthly variability of speed in the domain.

302





303 The presence of eddies relates to the transference from mean potential to mean kinetic energy, observed by the SSH 304 variability and MKE in Figure 7. The MKE pattern displays the highest values where the highest speed is placed, as 305 expected, but the variability in the SSH is observed only in the BMC (Figure 7d). The high-resolution benefits the 306 maintenance of the MKE distribution, particularly in the BMC, where the eddies are the major variability driver. To the west 307 of 55°W, the Patagonian Shelf circulation is guided by the interaction of semidiurnal and diurnal tidal components with the 308 bottom friction and wind stress (Palma et al., 2004, 2008). The speed of the currents in the southern Patagonian Shelf in the 309 model output represents this dynamical effect (Figure 6a). In other parts of the domain, the variability in the SSH is higher 310 only in the river mouth. This indicates the influence of barotropic tides, which intensely modify the SSH in shallower 311 regions. As it shows fewer SSH deviations, the propagation of eddies in the NBC in this simulation is reduced. 312 Distinguishing aspects found for each WBC are covered in the following sections. The MKE distribution and intensity of > 313 0.2 m²/s² are similar to observations (Oliveira et al., 2009), and the distribution agrees with reanalysis (Poli et al., 2022).

314 4. Seasonal Variability and Trends of the WBCs

315 4.1 Brazil-Malvinas Confluence

316 The BMC variability depends on mesoscale variability and eddy propagation, often diagnosed by the standard deviation of 317 the SSH. In Figure 6 the model patterns are consistent with those analyzed by Oliveira et al. (2009), using observed data 318 from drifting buoys interpolated onto a 0.5°x0.5° grid. The model also shows similarity with the observed MKE field from 319 other studies (Oliveira et al., 2009, Combes and Matano, 2014a) (Figure 7). Several authors have emphasized the importance 320 of wind stress in maintaining the barotropic component of the circulation of the northern Patagonian Shelf (Lago et al., 2019; 321 Campos et al., 2013; Palma et al., 2008, 2004; Combes and Matano, 2018). The most prominent influence is during the 322 well-mixed period (JJAS) rather than in the stratified period (JFMA), when the baroclinic component is more relevant (Lago 323 et al., 2019). This effect can be diagnosed in the climatological field in Figure 7. The presence of eddies in the annual 324 average enhances the standard deviation of SSH and reveals the baroclinic component. The barotropic component is related 325 to the total MKE distribution in the annual average in Figure 7c. It is confirmed that the main variability of the velocity fields 326 is related to eddy propagation, which drives the SSH variability. The model consistently preserves the circulation features of 327 the BMC even in regions close to shallow shelves.

328

329 The model captures the seasonal behavior of the BC and the MC, revealing the density variations through the seasons in 330 Figure 3. This implies that the MC takes a northern place during the colder seasons in this hemisphere (JJA, SON) while the 331 BC advances during the warmer seasons (DJF, MAM). This is also evident in the seasonal cycle of the BC and MC transport 332 (Figure 8) and in the number of extremes per season (Figure 10). The model registered below-average transport for the MC 333 from October through April and above-average transport from May through September. The BC has the opposite cycle, and 334 above-average southward transport occurs from December until April. The seasonal cycle is similar to what was found by





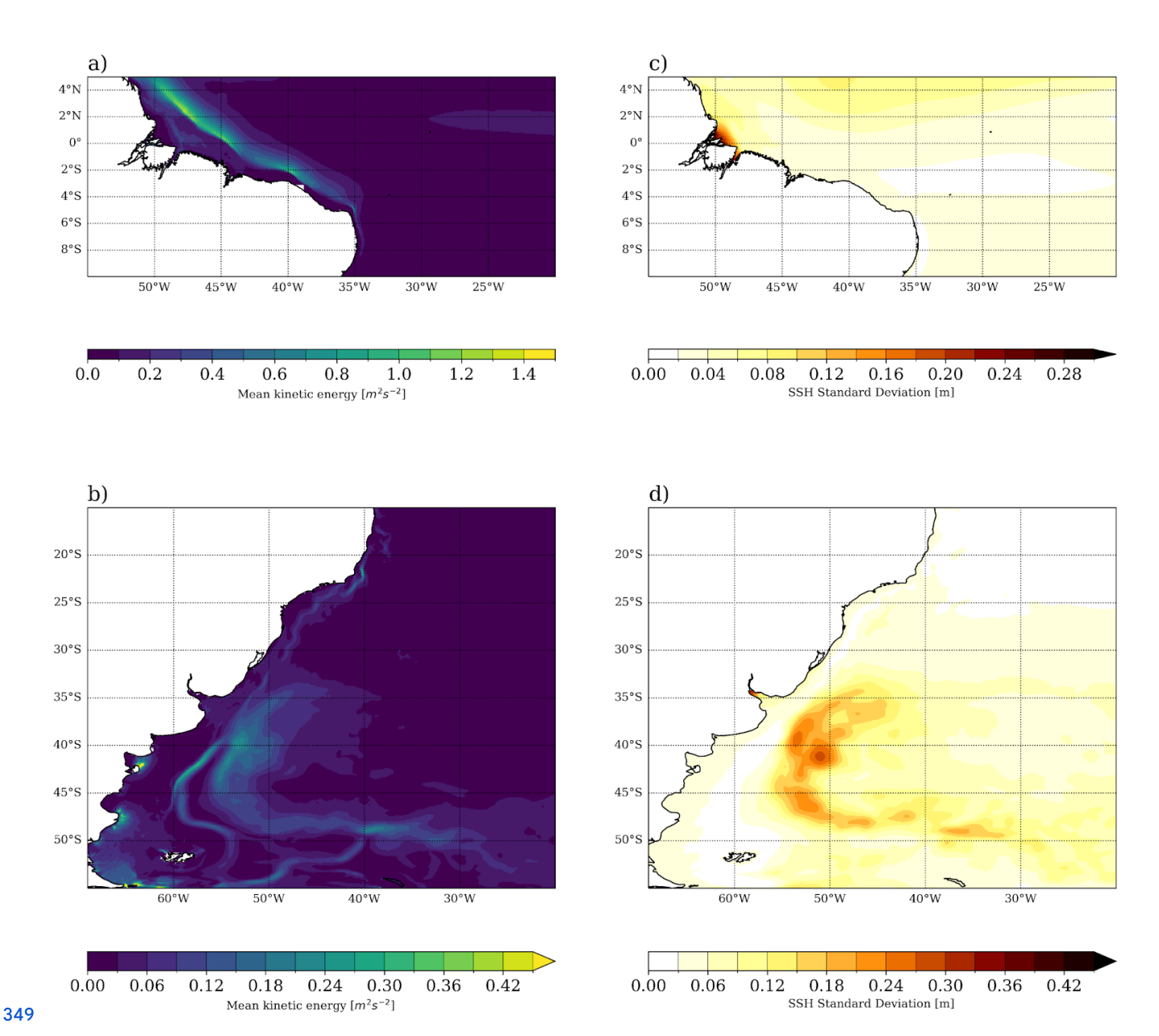
335 Combes and Matano (2014b) with ROMS simulations. Despite this, ROMS presents a higher MC mean transport of around 336 73.1 Sv at 41°S compared to MOM6's 60.3 Sv transport at 45°S (Figure 8). The BC transport is higher in this simulation, 337 around 57.9 Sv, while ROMS registers 40 Sv at 33°S.

338

349 The transport of the BC and MC shows a high interannual variability, as depicted in Figure 8. Different authors have 340 indicated that both currents can widely vary their transport from 5 to 88 Sv, with smaller transport in the BC (Goni et al., 341 2011). The increased MC transport induces the seasonal negative temperature bias in the 20-year mean temperature patterns 342 from MAM until SON (Figure 3). Besides, the transports show a negative trend, more than 10 times higher than the trend 343 obtained with observations (Goni et al., 2011). This could imply a systematic error in the simulation. Studies indicated that 344 adjustments in the model bottom friction modify the mean northern ACC transport, inducing changes in the mean BMC 345 (Combes and Matano, 2014a; Peterson, 1992; Combes and Matano, 2014b). As in this simulation, the ACC transport is given 346 through reanalysis data, the bottom friction is the parameter that could interfere with the MC variability. However, the BC 347 offers a balanced higher southward trend, which other studies have indicated as a consequence of Atlantic Ocean warming 348 (Lumpkin and Garzoli, 2011; Risaro et al., 2020).







350 Figure 7: Standard deviations of the Mean Kinetic Energy (m2s-2) (a,b) and SSH (m) (c,d) in the regions of the WBCs. In the 351 latter, fields are std concerning the monthly variability from 1997 until 2017.

352 Although the BMC separation occurs on average between the latitudes 37°S and 39°S (Goni et al., 2011), several studies 353 have recorded climatic trends of a southward shift in the BMC position. The trend is induced by the intense warming 354 observed in this ocean (Risaro et al., 2022; Franco et al., 2020), but the intensity of this relation and variability is still 355 uncertain. According to Goni et al. (2011), with satellite observations, this trend has a rate of 1.5° per decade between 356 1993-2008. Lumpkin and Garzoli (2011) indicated a varying rate between 0.6 to 0.9° per decade with data from 1992 until





357 2007. A numerical model used by Combes and Matano (2014b) revealed a displacement of 0.62° per decade, which the 358 study related to the weakening of the ACC.

359

360 The BMC separation obtained from model outputs is the latitude where the 1000 m isobath meets the 10°C isotherm at 200 361 m, which, according to Garzoli and Bianchi (1987), depicts a location of enhanced time-space variability of the front 362 separation. For the 20-year MOM6 simulation, the mean BMC separation is at $36.76^{\circ}\text{S} \pm 0.77^{\circ}$, as depicted in Figure 2. The 363 plot shows the mean position obtained with Glorys for the same period and by Goni et al. (2011), which considered satellite 364 observations from 1993 until 2008. The model simulation is slightly ($\approx 1^{\circ}$) more northerly than the other estimates in the 365 plot. Using ROMS, Combes and Matano (2014b) estimate that the BMC separation is $\approx 2^{\circ}$ farther south, around 39°S.

366

367 The 20-year simulation outputs allow for the characterization of trends in this ocean, which is important for diagnosing the 368 variability of the mean state. The model overestimated the BMC separation trend over the years compared to observations. 369 The simulation registers a -0.93°/decade deviation, while Goni et al. (2011) obtained different results based on observations 370 of SST and SSH, with values of -0.39° and -0.81° per decade, respectively. Lumpkin and Garzoli (2011) indicate a trend 371 between 0.6 and 0.9°/decade for 1992-2007. Despite the higher trend, the model mean BMC separation is close to other 372 estimates (Figure 2), indicating that the model seasonal bias is compensated and the MC positioning is stable in this 373 simulation.

374

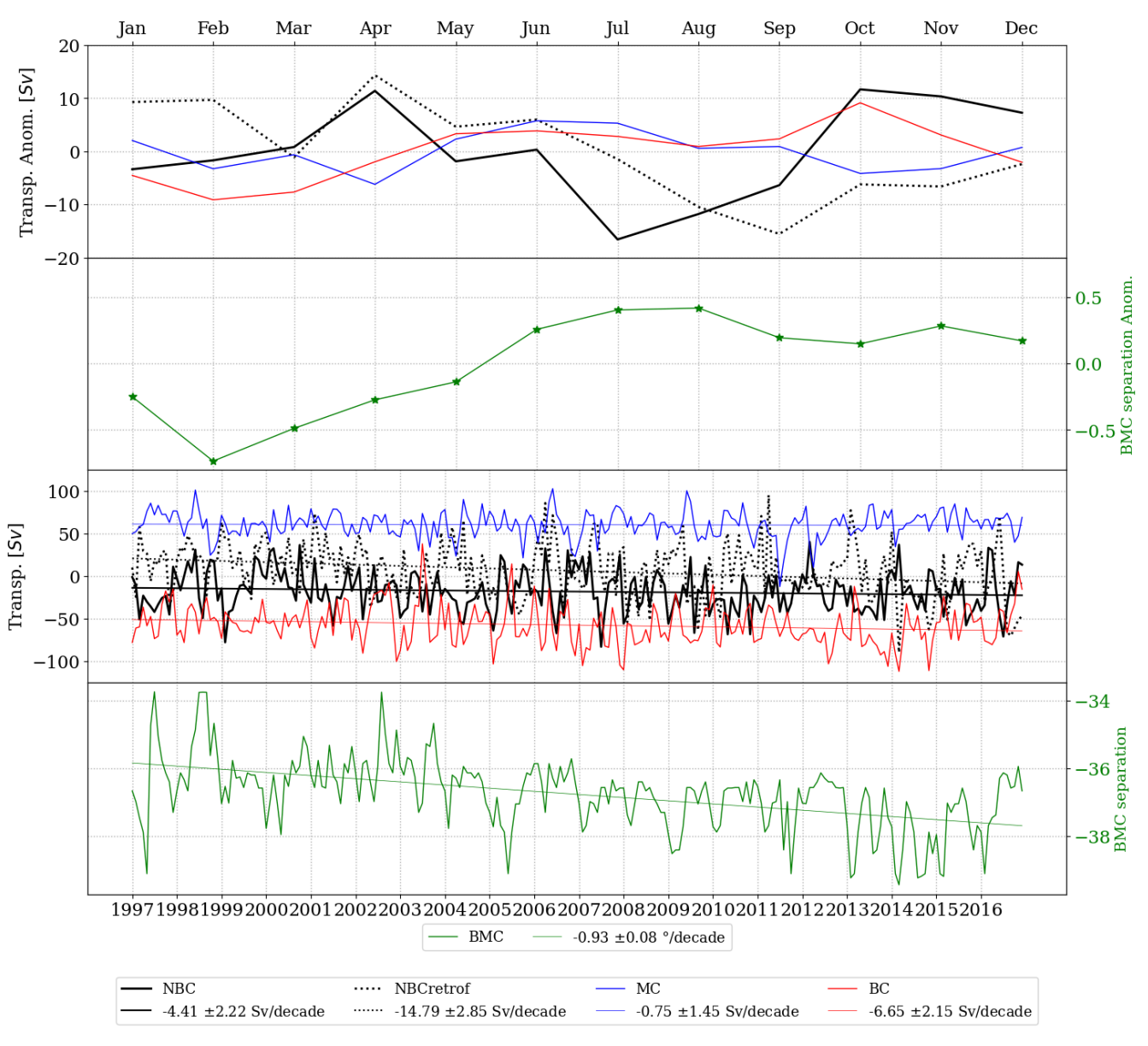
375 The trends of surface variables in Figure 9 depict important patterns in the BMC region. The temperature in the BMC is very 376 similar to the pattern obtained with satellite observations for the 1982–2017 period (Risaro et al., 2020). The temperature is 377 warmer in most BMC vicinities, while it is cooler in the southern part of the domain, representing more than 0.5 std. 378 Enhancing the polar northward flow from the Drake Passage contributes to the negative SST and SSS trend, resulting in 379 fresher and colder waters. In the BMC region, surface speed trends present a similar pattern; accordingly, warmer and saltier 380 waters are faster and have increased transport, while colder and fresher waters are slower. This agrees with the number of 381 BMC separation location extremes in Figure 10, which reduces significantly through the years, confirming the southward 382 movement. In a warmer environment, the transport generated by the BMC presents stronger initial energy, but its track has a 383 southward displacement.

384

385 Concerning the patterns far from the coast, there is a warming longitudinal trend pattern at 35°S extending from 35°W until 386 15°W, evident in the model but not in the observations (Risaro et al., 2020). The region is known for its constant westward 387 flow and propagation of eddy from the Agulhas Current (Guerra et al., 2018). This indicates an intensification of the 388 transport to the north of 35°S in comparison to what is observed farther south.







391 Figure 8: Ocean transport of the WBCs in the domain and the latitudinal displacement of the BMC separation. The first row 392 shows the mean monthly transport anomalies for each WBC, and the second row shows the mean monthly BMC separation 393 anomalies. The third row depicts the interannual transport for the WBC, and the bottom row shows the BMC positioning. The 394 ocean transport is vertically integrated between latitudes 0° and 3.5°N for the NBC and 4° and 5°N for its retroflection, whereas it 395 is at latitudes 45°S and 33°S for the MC and BC, respectively. The transects are depicted in Figure 2. The positive transport flows 396 northward and east, and the negative transport flows south and west.





397 4.2 North Brazil Current

398 The NBC presents high variability associated with the propagation of eddies (Bueno et al., 2022; Garzoli et al., 2004). The 399 model, however, underestimates the SSH variability in the NBC retroflection, which suggests there is weaker transport from 400 the SEC to the NBC. Some authors use zonal transport estimates based on NBC propagation and retroflection sections to 401 verify this diagnosis (Garzoli et al., 2004). The region is marked by intense currents, registering transport of 16 ± 2 Sv for 402 the NBC and 22 ± 2 Sv for the retroflection obtained by Garzoli et al. (2004). Accordingly, the estimates for the same 403 sections with MOM6 outputs indicate that the 20-year average transport is around 18.4 Sv for the NBC. For its retroflection, 404 however, the transport series initiated with an amount of 22Sv but indicated an average of 5.9 Sv. Garzoli et al. (2004) 405 considered a 15-month mean by local sounders measurements, registering a seasonal cycle with more intense transport 406 during ASO, less intense during MAM for the NBC, and the opposite for its retroflection. The MOM6 simulation fails to 407 reproduce any of these characteristics for the retroflection (Figure 8a).

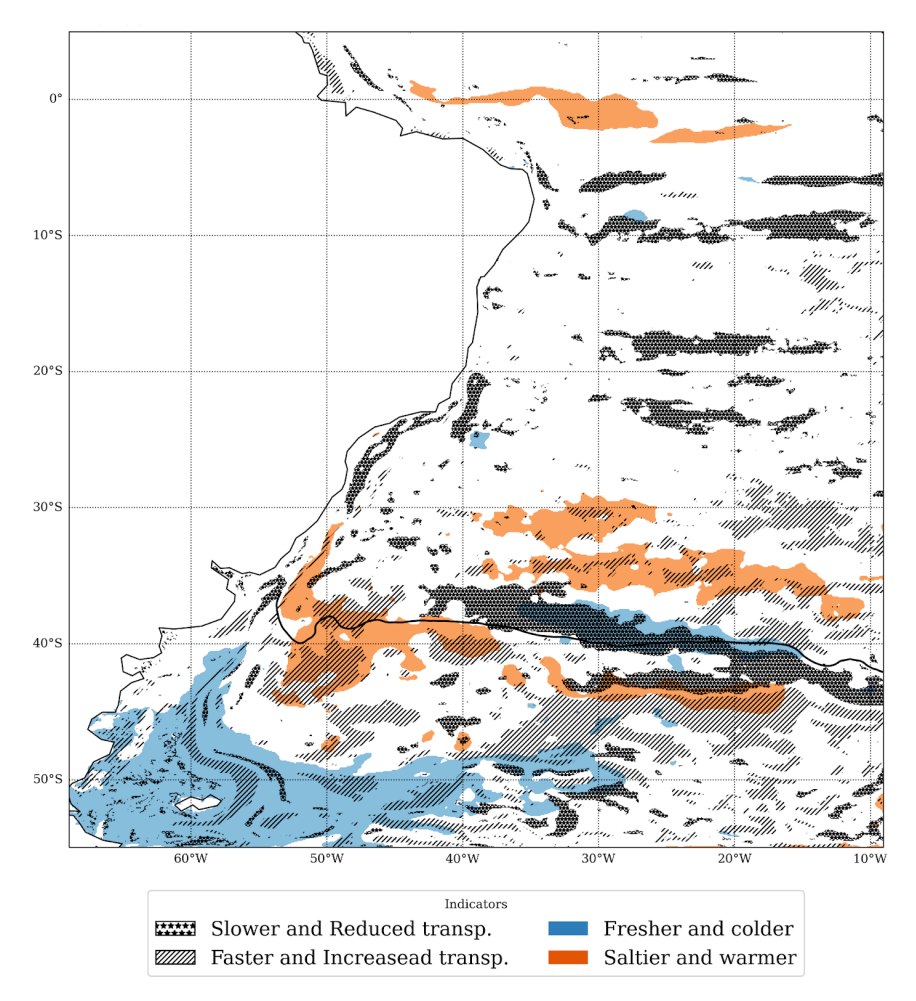
408

With maximum latitude at 5°N, this simulation cannot fully develop the NBC retroflection and its eddies since its natural 410 path can deviate from 4°N to 8°N (Bueno et al., 2022; Valerio et al., 2021). Accordingly, the negative trend of the NBC 411 retroflection indicates that NBC reduced its transport but changed its path through the years and relocated outside the 412 model's domain. Despite that, features like temperature, salinity, and transport of the currents in the NBC region are 413 precisely described during MAM. The bias appearing during JJA is maintained through the colder seasons (Figure 3). This 414 represents the lack of mixing, which can be either due to the influence of the wind speed (Figure 5c) or the use of a 415 z-coordinate vertical structure. Another limiting factor is the wind intensity, which contributes to wind stress and mixing. 416 Reduced wind speed has proven insufficient for mixing and could lead to reduced eddy formation, thereby reducing the 417 seasonal NBC retroflection transport.



423





419 Figure 9: Trends in the WBCs. Trends of different surface variables simulated by the model. Trends originate from a 36-month 420 running mean smothered series of standardized anomalies (Risaro et al., 2020). Colored regions are significant at a 95% 421 confidence level, according to Mann-Kendall's test. The trends by decade are normalized, and the colors display anomalous 422 patterns above 0.5 std.

Although this simulation cannot fully represent the development of the NBC retroflection, investigating this deviation is crucial to determine the variability of some climate patterns in the equatorial region, such as the storm track, the AMOC, and the ITCZ. The absence of eddy propagation (Figure 7) and transport (Figure 8) in the region, for instance, might indicate deviation in the dynamical structure of the model. Nevertheless, the model conserves large-scale SEC transport since the mean NBC eastward transport resembles values slightly closer than those obtained from local measurements (Garzoli et al., 2004). Still, many other factors could disfavor the propagation of NBC eddies. The proximity to the northern boundary is a critical limiting factor, since this front could change its position through the years. However, it is also important to indicate that the negative trend observed in the region can be related to atmospheric mechanisms and trends.





432

433 The trends in Tropical Atlantic Ocean waters indicate elevated temperature and salinity, as shown in Figure 9. This trend is 434 not associated with transport and speed patterns. The Amazon River flow increases the transport and current speed in the 435 northwestern part of the domain. The merged patterns of current speed and transport attenuate the eccentricity of the currents 436 in the region, as revealed in Figure 8b. Thus, while the North Brazil Current (NBC) and its retroflection experience a 437 reduction in transport, they exhibit an increase in speed. The lack of stratification, as shown in Figure 4, suggests an 438 inefficient transport of momentum to the sub-surface layers. This may also be influenced by external forcings or the 439 redistribution of flow pathways out of the domain.

440 4.3 Evaluation of external and internal forcings

The WBCs in the Southwestern Atlantic domain feature intense variability and trends. This has been indicated by trends in the mean state of the surface variables (Figure 9), along with a tendency toward reduced extreme transport (Figure 10). Furthermore, extreme transports in the BC/MC are associated with the displacement of the BMC. In 1998, a year of an elevated number of extreme BMC displacements, the signal that enhances the southward movement of the BMC is unrelated to the transport amount toward the region. Thus, external teleconnections also generate modulations of the currents in the region. This section further investigates the components of this modulation.

447

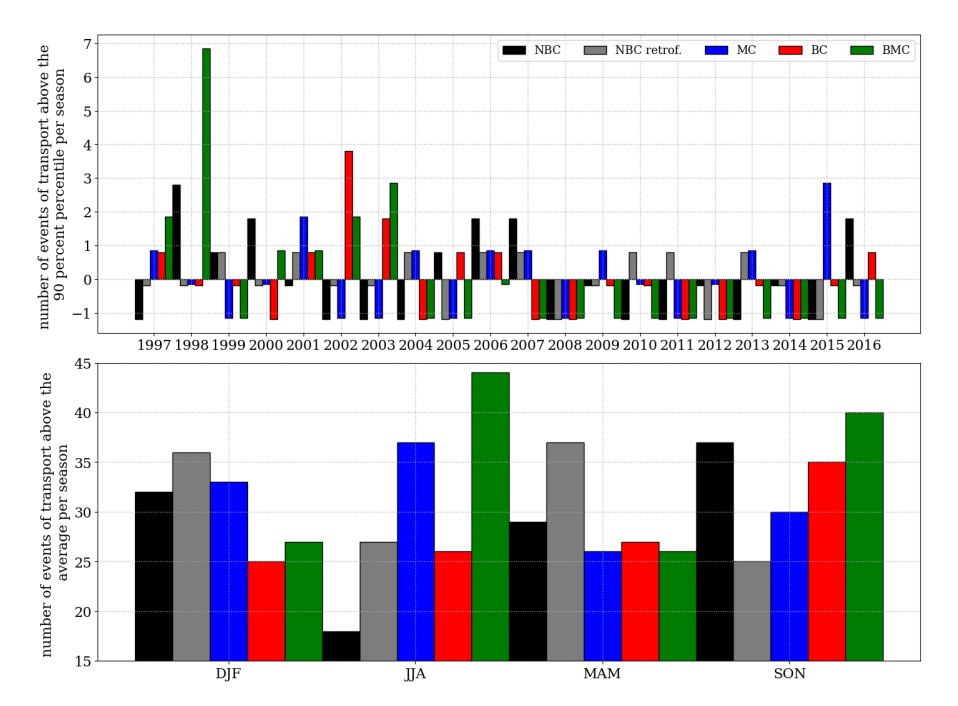
External forcing, such as atmospheric teleconnections, can explain the mixed signals of the trend, indicating that the influence is not driven strictly by local forcings. Combes and Matano (2018) observed that the La Plata Basin flows are linked to the interannual variability of the ENSO. The correlation coefficients between the WBCs and climate indices indicate the susceptibility of the MC to Eastern Pacific Ocean variability, with significant correlation between its transport and the Nino1.2 and the PDO indices of 0.14 and 0.18, respectively. The BMC also presents a significant correlation of 0.26 with the Nino1.2 index. These relations combine tropical and extratropical teleconnections with atmospheric components that drive turbulence and freshwater discharge in the domain. The result is strong MC and northern BMC in response to the tripical temperatures in the Eastern Pacific.



459

466





457 Figure 10: Registries of extreme transport events in the WBCs. The graphics show the events from 1997 to 2016 with transport 458 above the 90 percent percentile per year (top) and above the average per season (bottom).

Due to the proximity to the coastal slopes, the internal variability of the currents and transport in the WBCs results in a definition of dynamic interactions, different from those in the open ocean (Hughes et al., 2019). The wave propagation from tropical regions in the Pacific follows the western South American coastline, which propagates and contributes to the coastal dynamics in the Southwest Atlantic Ocean. Poli et al. (2022) reveal that Kelvin wave dispersion and Rossby wave propagation from the Madden-Julian Oscillation are linked to the barotropic and baroclinic components of the coastal trapped waves in the Southwest Atlantic Ocean.

467 To examine the waves occurring on the coastline in the model outputs, we plot a dispersion diagram following Wheeler and 468 Kiladis (1998). The diagram reveals the spectrum eccentricity of a determined location at a determined period in time, 469 enabling the dynamic patterns to be classified by frequency and wavenumbers. Figure 11 displays the distinctive patterns 470 during two distinct behaviors of the BMC separation: southern and northern extreme shifts. The wave patterns indicate that 471 this region is influenced by coastal and open ocean dynamics. The low-frequency energy waves of positive and negative 472 wavenumbers reveal the influence of eastward and westward Rossby wave propagation. The westward pattern can be driven 473 by MJO propagation (Poli et al., 2022), while the eastward pattern is a response to the Indian Ocean Rossby Wave 474 propagation from the Agulhas Current. Another important pattern is the higher-frequency modes, whose behavior is similar 475 to that of inertial gravity waves, and we associate this pattern with the coastal trapped wave disturbance. Despite the high



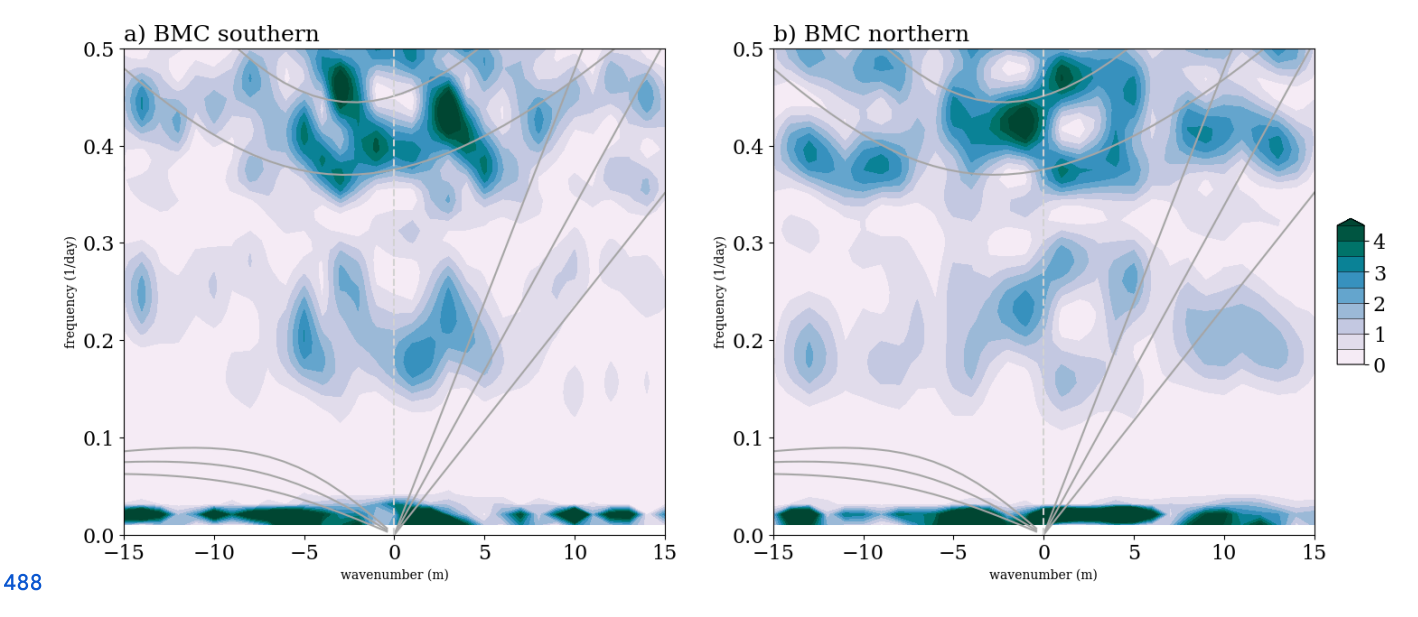


476 frequency, the inertial gravity waves in this region have shorter wavelengths. Thus, the propagation is constrained in the 477 region and is mainly affected by wind stress, bottom topography, and interactions with other wave patterns. Their 478 propagation relies on variations in density and temperature on the ocean surface due to wind forcing. The most important 479 aspect of this pattern in the region is the interaction of inertial gravity waves with the mesoscale and submesoscale motions 480 (Alford et al., 2016).

481

482 The different energy spectra occur during the distinct events for mid-frequency waves, which in the theory are classified as 483 mixed gravity-Rossby Waves and Kelvin Waves (Figure 11). The propagation of Kelvin Waves also relates to external 484 forcing from equatorial sources (Hughes et al., 2019; Poli et al., 2022). The diagram shows that its energetic disturbance 485 contributes to northern BMC displacement, which is explained by the northward propagation of these features. This result 486 increases the understanding of the drivers of extreme shifts in the BMC separation.

487



489

490 Figure 11: Frequency and wavenumber diagram during extreme meridional displacement of the BMC separation: a) BMC 491 southern, b) BMC northern. The spectrum reveals the frequency and wavenumber in the model SSH outputs band-pass series 492 filtered between 40 and 130 days for the 300 m isobath between latitudes 20°S and 50°S.





494 5. Summary and Conclusions

495 This work analyzed the representation of the Southwestern Atlantic circulation using a 20-year MOM6 simulation at a 7 km 496 resolution, focusing on the variability of the WBCs. The results first explore the performance of the simulation, which has 497 proven to be skillful when compared to observational and reanalysis datasets. The Eddy-permitting resolution allows a better 498 representation of the SST and SSS fields than coarser resolution simulations. The model accurately captured surface ocean 499 circulation and temperature and salinity gradients. The maximum negative SST bias of 1.0°C is sufficiently good 500 performance for forecasting ocean conditions. The correspondence between density and MLD to the salinity and temperature 501 structure indicates that the model reproduces thermodynamic effects fairly. Their effects on the density field drive the 502 large-scale circulation, as highlighted by the global circulation and mesoscale features.

503

The transport of the currents in the simulation has evolved over decades in the Southwestern Atlantic WBCs. The BMC separation is a region with stronger kinetic energy in the domain. Observing the components of the BMC variability can help identify the location of eddy propagation and shelfbreak upwelling. Although it has been related to the bottom drag, the enhanced southward shift in the BMC is also consistent with the heating trend in this study. The warming Atlantic is followed by a modified BC transport with an increase of 6.65 ± 2.15 Sv in the southward flow per decade. This feature is usually balanced by the conservation of the MC transport. The trends show enhanced northward transport of fresher and colder waters from the ACC, which reduces the temperature by bringing cool waters to the region. Despite this, the trends modify the location of the BMC separation, with a southward displacement of 0.93 ± 0.08 °/decade.

512

We show that the location of the BMC separation has extremes that relate to natural climate variability patterns in the Pacific Ocean. The Pacific Ocean warming has a stronger correlation and enhanced activity during MC transport extremes and northward BMC. The Nino1.2 (East Niño) and PDO indices corroborate this behavior. The impacts are explained by a spectral analysis, which reveals Rossby and Kelvin Wave-like disturbances, in addition to the inertial gravity waves intrinsic in the slope proximity. Eastward and westward propagating Rossby waves occur as a link between tropical disturbances such as the MJO and the Agulhas Current (Guerra et al., 2018; Poli et al., 2022). The Kelvin wave disturbances appear to be positioning as they propagate northward. This indicates that although the warmer Atlantic enhances the southward shift in the BMC separation, mechanisms intensified by the warmer Eastern Pacific can enhance the northward flow.

522

523 The NBC also presents reduced transport, but the model has captured a higher negative trend than that of the one in the BC. 524 The unbalanced reduction of 14.79 ± 2.85 Sv per decade for its retroflection weakly correlates with natural climate 525 variability patterns. Still, other contributing factors can explain the intense influences observed in the NBC activity. We 526 found that the transport trends occur alongside a positive current speed trend. Since much of the variability of the ocean





527 surface currents receives a direct contribution from the wind, weaker winds lead to reduced NBC eastward propagation with 528 fewer eddies. Along with the absence of winds, we show a reduced stratification pattern commonly linked to lower 529 temperatures and, consequently, the transport in adjacent layers. Additionally, the reduced transport registered by the model 530 in the tropical regions could be associated with the proximity to the northern boundaries and the modification of flow 531 pathways, which should be addressed in future research.

532

533 The coordinate system is also relevant to the deviated stratification structure captured by the model in the equatorial region.

534 Studies have indicated that the reduced mixing in the ocean interior is inherent to vertical z-coordinate system models,

535 especially in highly stratified regions (Adcroft et al., 2019; Griffies et al., 2000). This could contribute to the bias found in

536 the equatorial and Amazonian regions but also can lead to the lack of mixing in the La Plata basin outflow region.

537

538 The analysis of the model output has proven helpful in diagnosing how the WBC dynamics are expected to vary under a

539 changing climate. We suggest that future experiments evaluate the efficiency of other coordinate systems in this domain. The

540 displacement of such energetic regions can cause tremendous impacts on marine ecosystems. We advise future research to

541 integrate a biogeochemistry model to diagnose this interaction specifically. Furthermore, an analysis comprising the

542 atmospheric feedback under the displaced WBCs is also recommended, as the Southwestern Atlantic Ocean presents an

543 important relationship with atmospheric systems (Laureanti et al., 2024).

544

545

546 Code and Data Availability. The datasets used for model validation and comparison are listed as follows: mixed-layer depth

547 (https://mld.ifremer.fr/Surface Mixed Layer Depth.php, De Boyer Montéut et al., 2004), QSCAT wind speed

548 (https://podaac.jpl.nasa.gov/QuikSCAT?tab=-mission-objectives§ions=about%2Bdata, Hoffman and Leidner, 2005),

549 PIRATA (https://www.pmel.noaa.gov/gtmba/pmel-theme/atlantic-ocean-pirata, Servain et al., 1998) and World Ocean Atlas

550 2023 (https://www.ncei.noaa.gov/access/metadata/landing-page/bin/iso?id=gov.noaa.nodc:NCEI-WOA23, Reagan et al.,

551 2023).

552

553 The datasets used to create the model forcing are listed as follows: GLORYS12 reanalysis

554 (https://doi.org/10.48670/moi-00021, Global Ocean Physics Reanalysis, 2021), TPXO9 (https://www.tpxo.net/home, Egbert

555 and Erofeeva, 2002), GloFAS (https://doi.org/10.24381/cds.a4fdd6b9, Zsoter, 2019), GEBCO (https://download.gebco.net/,

556 Giribabu et al., 2023) SeaWIFS (https://oceandata.sci.gsfc.nasa.gov/, NASA, 2018) and ERA5

557 (https://cds.climate.copernicus.eu/datasets, Hersbach et al., 2023). The model source code is uploaded in

558 https://zenodo.org/records/17252994 and scripts for setting-up are in https://zenodo.org/records/17252554. The model

559 outputs are available under the link

560 http://antares.esm.rutgers.edu:8080/thredds/catalog/MOM6/ESMG/SWA14/exp.010/catalog.html





562 *Author contributions.* The authors contributed equally to this work.

563

564 *Competing interests.* The authors declare no conflict of interest.

565

- 566 Acknowledgements. The authors thank the Coordenação de Aperfeiçoamento de Pessoal de Nível Superior (CAPES) Finance
- 567 Code 001 for its financial support and the Earth System Modelling Laboratory at Rutgers University.
- 568 Part of this work used resources from the Centro Nacional de Processamento de Alto Desempenho em São Paulo
- 569 (CENAPAD-SP) in Brazil and also the high-performance computing support from Cheyenne (doi:10.5065/D6RX99HX)
- 570 provided by NCAR's Computational and Information Systems Laboratory, sponsored by the National Science Foundation.
- **571** SCC thanks CNPq for the grant no. 312742/2021-5.

572 6. References

- 573 Adcroft, A. and Campin, J.-M.: Rescaled height coordinates for accurate representation of free-surface flows in ocean
- 574 circulation models, Ocean Modelling, 7, 269–284, https://doi.org/10.1016/j.ocemod.2003.09.003, 2004.
- 575 Adcroft, A., Anderson, W., Balaji, V., Blanton, C., Bushuk, M., Dufour, C. O., Dunne, J. P., Griffies, S. M., Hallberg, R.,
- Harrison, M. J., Held, I. M., Jansen, M. F., John, J. G., Krasting, J. P., Langenhorst, A. R., Legg, S., Liang, Z., McHugh, C.,
- 577 Radhakrishnan, A., Reichl, B. G., Rosati, T., Samuels, B. L., Shao, A., Stouffer, R., Winton, M., Wittenberg, A. T., Xiang,
- 578 B., Zadeh, N., and Zhang, R.: The GFDL Global Ocean and Sea Ice Model OM4.0: Model Description and Simulation
- 579 Features, Journal of Advances in Modeling Earth Systems, 11, 3167–3211, https://doi.org/10.1029/2019MS001726, 2019.
- 580 Aiki, H., Zhai, X., and Greatbatch, R. J.: Energetics of the global ocean the role of mesoscale eddies, chap. 4, pp. 109–134,
- 581 https://doi.org/10.1142/9789814696623 0004, 2015.
- 582 Alford, M. H., MacKinnon, J. A., Simmons, H. L., and Nash, J. D.: Near-Inertial Internal Gravity Waves in the Ocean.
- 583 Annual review of marine science, 8, 95-123, 2016.
- 584 Bonou, F. K., Noriega, C., Lefèvre, N., & Araujo, M.: Distribution of CO2 parameters in the Western Tropical Atlantic
- 585 Ocean. Dynamics of Atmospheres and Oceans, 73, 47–60. https://doi.org/10.1016/J.DYNATMOCE.2015.12.001, 2016.
- 586 Brum, A. L., de Azevedo, J. L. L., de Oliveira, L. R., and Calil, P. H. R.: Energetics of the Brazil Current in the Rio Grande
- 587 Cone region, Deep Sea Research Part I: Oceanographic Research Papers, 128, 67–81,
- 588 https://doi.org/10.1016/J.DSR.2017.08.014, 2017.
- 589 Bueno, L. F., Costa, V. S., Mill, G. N., and Paiva, A. M.: Volume and Heat Transports by North Brazil Current Rings,
- 590 Frontiers in Marine Science, 9, https://doi.org/10.3389/fmars.2022.831098, 2022.
- 591 Campos, P. C., Möller, O. O., Piola, A. R., and Palma, E. D.: Seasonal variability and coastal upwelling near Cape Santa
- 592 Marta (Brazil), Journal of Geophysical Research: Oceans, 118, 1420–1433, https://doi.org/10.1002/JGRC.20131, 2013.





- 593 Chassignet, E. P. and Xu, X.: On the Importance of High-Resolution in Large-Scale Ocean Models,
- 594 https://doi.org/10.1007/s00376-021-0385-7, 2021.
- 595 Combes, V. and Matano, R. P.: A two-way nested simulation of the oceanic circulation in the Southwestern Atlantic, Journal
- 596 of Geophysical Research: Oceans, 119, 731–756, https://doi.org/10.1002/2013JC009498, 2014a.
- 597 Combes, V. and Matano, R. P.: Trends in the Brazil/Malvinas Confluence region, Geophysical Research Letters, 41,
- 598 8971–8977, https://doi.org/10.1002/2014GL062523, 2014b.
- 599 Combes, V. and Matano, R. P.: The Patagonian shelf circulation: Drivers and variability, Progress in Oceanography, 167,
- **600** 24–43, https://doi.org/10.1016/J.POCEAN.2018.07.003, 2018.
- 601 de Boyer Montégut, C., Madec, G., Fischer, A. S., Lazar, A., and Iudicone, D.: Mixed layer depth over the global ocean: An
- 602 examination of profile data and a profile-based climatology, Journal of Geophysical Research: Oceans, 109,
- 603 https://doi.org/10.1029/2004JC002378, 2004.
- 604 Egbert, G. D. and Erofeeva, S. Y.: Efficient Inverse Modeling of Barotropic Ocean Tides, Journal of Atmospheric and
- 605 Oceanic Technology, 19, 183 204,
- 606 https://doi.org/https://doi.org/10.1175/1520-0426(2002)019<0183:EIMOBO>2.0.CO;2, 2002.
- 607 Fox-Kemper, B., Danabasoglu, G., Ferrari, R., Griffies, S. M., Hallberg, R. W., Holland, M. M., Maltrud, M. E., Peacock, S.,
- 608 and Samuels, B. L.: Parameterization of mixed layer eddies. III: Implementation and impact in global ocean climate
- 609 simulations, Ocean Modelling, 39,61–78, https://doi.org/10.1016/j.ocemod.2010.09.002, modelling and Understanding the
- 610 Ocean Mesoscale and Submesoscale, 2011.
- 611 Franco, B. C., Defeo, O., Piola, A. R., Barreiro, M., Yang, H., Ortega, L., Gianelli, I., Castello, J. P., Vera, C., Buratti, C.,
- 612 Pájaro, M., Pezzi, L. P., and Möller, O. O.: Climate change impacts on the atmospheric circulation, ocean, and fisheries in
- 613 the southwest South Atlantic Ocean: a review, Climatic Change, 162, 2359–2377,
- 614 https://doi.org/10.1007/S10584-020-02783-6, 2020.
- 615 Garzoli, S. L. and Bianchi, A.: Time-space variability of the local dynamics of the Malvinas-Brazil confluence as revealed
- 616 by inverted echosounders, Journal of Geophysical Research: Oceans, 92, 1914–1922,
- 617 https://doi.org/https://doi.org/10.1029/JC092iC02p01914, 1987.
- 618 Garzoli, S. L. and Matano, R.: The South Atlantic and the Atlantic Meridional Overturning Circulation, Deep Sea Research
- 619 Part II: Topical Studies in Oceanography, 58, 1837–1847, https://doi.org/10.1016/j.dsr2.2010.10.063, climate and the
- 620 Atlantic Meridional Overturning Circulation, 2011.
- 621 Garzoli, S. L., Ffield, A., Johns, W. E., and Yao, Q.: North Brazil Current retroflection and transports, Journal of
- 622 Geophysical Research: Oceans, 109, https://doi.org/10.1029/2003JC001775, 2004.
- 623 Giribabu, D., Hari, R., Sharma, J., Ghosh, K., Padiyar, N., Sharma, A., Bera, A. K., and Srivastav, S. K.: Assessment of
- 624 GEBCO 2023 Gridded Bathymetric Data in Shallow Waters Using the Seafloor from ICESat-2 Photons, Preprint to Marine
- 625 Geophysical Research, 2023, https://doi.org/10.21203/rs.3.rs-3020167/v1, 2023.





- 626 Goni, G. J., Bringas, F., and DiNezio, P. N.: Observed low frequency variability of the Brazil Current front, Journal of
- 627 Geophysical Research: Oceans, 116, https://doi.org/10.1029/2011JC007198, 2011.
- 628 Griffies, S. M., Böning, C., Bryan, F. O., Chassignet, E. P., Gerdes, R., Hasumi, H., Hirst, A., Treguier, A.-M., and Webb, D.:
- 629 Developments in ocean climate modelling, Ocean Modelling, 2, 123–192,
- 630 https://doi.org/https://doi.org/10.1016/S1463-5003(00)00014-7, 2000.
- 631 Griffies, S. M., Winton, M., Anderson, W. G., Benson, R., Delworth, T. L., Dufour, C. O., Dunne, J. P., Goddard, P.,
- 632 Morrison, A. K., Rosati, A., Wittenberg, A. T., Yin, J., and Zhang, R.: Impacts on ocean heat from transient mesoscale
- eddies in a hierarchy of climate models, Journal of Climate, 28, 952–977, https://doi.org/10.1175/JCLI-D-14-00353.1,
- **634** 2015.
- 635 Guerra, L. A. A., Paiva, A. M., Chassignet, E. P.: On the translation of Agulhas rings to the western South Atlantic Ocean,
- 636 Deep-Sea Research Part I, 139, 104–113, 2018.
- 637 Guerrero, R. A., Piola, A. R., Fenco, H., Matano, R. P., Combes, V., Chao, Y., James, C., Palma, E. D., Saraceno, M., and
- 638 Strub, P. T.: The salinity signature of the cross-shelf exchanges in the Southwestern Atlantic Ocean: Satellite observations,
- 639 Journal of Geophysical Research: Oceans, 119, 7794–7810, https://doi.org/10.1002/2014JC010113, 2014.
- 640 Hallberg, R.: Using a resolution function to regulate parameterizations of oceanic mesoscale eddy effects, Ocean Modelling,
- 641 72, 92–103, https://doi.org/10.1016/j.ocemod.2013.08.007, 2013.
- 642 Hersbach, H., Bell, B., Berrisford, P., Biavati, G., Horányi, A., Muñoz Sabater, J., Nicolas, J., Peubey, C., Radu, R., Rozum,
- 643 I., Schepers, D., Simmons, A., Soci, C., Dee, D., Thépaut, J-N. (2023): ERA5 hourly data on single levels from 1940 to
- present. Copernicus Climate Change Service (C3S) Climate Data Store (CDS), DOI: 10.24381/cds.adbb2d47 (Accessed on
- 645 24-Jan-2025)
- 646 Hoffman, R. N. and Leidner, S. M.: An Introduction to the Near–Real–Time QuikSCAT Data, Weather and Forecasting, 20,
- 647 476 493, https://doi.org/https://doi.org/10.1175/WAF841.1, 2005.
- 648 Hughes, C.W., Fukumori, I., Griffies, S.M., Huthnance, J.M., Minobe, S., Spence, P., Thompson, K.R., Wise, A.: Sea
- 649 Level and the Role of Coastal Trapped Waves in Mediating the Influence of the Open Ocean on the Coast. Surv. Geophys.,
- 650 40, 1467–1492, https://doi.org/10.1007/s10712-019-09535-x, 2019
- 651 Jackson, L., Hallberg, R., and Legg, S.: A Parameterization of Shear-Driven Turbulence for Ocean Climate Models, Journal
- 652 of Physical Oceanography, 38, 1033 1053, https://doi.org/https://doi.org/10.1175/2007JPO3779.1, 2008.
- 653 Jean-Michel, L., Eric, G., Romain, B.-B., Gilles, G., Angélique, M., Marie, D., Clément, B., Mathieu, H., Olivier, L. G.,
- 654 Charly, R., Tony, C., Charles-Emmanuel, T., Florent, G., Giovanni, R., Mounir, B., Yann, D., and Pierre-Yves, L. T.: The
- 655 Copernicus Global 1/12° Oceanic and Sea Ice GLORYS12 Reanalysis, Frontiers in Earth Science, 9,
- 656 https://doi.org/10.3389/feart.2021.698876, 2021.
- 657 Kang, D., Curchitser, E. N., and Rosati, A.: Seasonal Variability of the Gulf Stream Kinetic Energy, Journal of Physical
- 658 Oceanography, 46, 1189 1207, https://doi.org/https://doi.org/10.1175/JPO-D-15-0235.1, 2016.
- 659 Kendall, M. G. Rank Correlation Methods, 4th edition, Charles Griffin, London, 1975.





- 660 Lago, L. S., Saraceno, M., Martos, P., Guerrero, R. A., Piola, A. R., Paniagua, G. F., Ferrari, R., Artana, C. I., and Provost,
- 661 C.: On the Wind Contribution to the Variability of Ocean Currents Over Wide Continental Shelves: A Case Study on the
- 662 Northern Argentine Continental Shelf, Journal of Geophysical Research: Oceans, 124, 7457–7472,
- 663 https://doi.org/10.1029/2019JC015105, 2019.
- 664 Laureanti, N. C., Chou, S. C., Nobre, P., and Curchitser, E.: On the relationship between the South Atlantic Convergence
- 665 Zone and sea surface temperature during Central-East Brazil extreme precipitation events, Dynamics of Atmospheres and
- 666 Oceans, 105, 10.1016/j.dynatmoce.2023.101422, 2024.
- 667 Locarnini, R., Mishonov, A., Baranova, O., Boyer, T., Zweng, M., Garcia, H., Reagan, J., Seidov, D., Weathers, K., Paver,
- 668 C., Smolyar, I., and Locarnini, R.: World Ocean Atlas 2018, Volume 1: Temperature, 2019.
- 669 Lumpkin, R. and Garzoli, S.: Interannual to decadal changes in the western South Atlantic's surface circulation, Journal of
- 670 Geophysical Research: Oceans, 116, https://doi.org/10.1029/2010JC006285, 2011.
- 671 Lumpkin, R. and Garzoli, S. L.: Near-surface circulation in the Tropical Atlantic Ocean, Deep Sea Research Part I:
- 672 Oceanographic Research Papers, 52, 495–518, https://doi.org/10.1016/J.DSR.2004.09.001, 2005.
- 673 Mann, H. B. Non-parametric tests against trend, Econometrica 1945, 13, 163-171.
- 674 Marcello, F., Tonelli, M., Ferrero, B., and Wainer, I.: Projected Atlantic overturning slow-down is to be compensated by a
- 675 strengthened South Atlantic subtropical gyre, Communications Earth & Environment 2023 4:1, 4, 1–15,
- 676 https://doi.org/10.1038/s43247-023-00750-4, 2023.
- 677 Mason, E., Pascual, A., Gaube, P., Ruiz, S., Pelegrí, J. L., and Delepoulle, A.: Subregional characterization of mesoscale
- 678 eddies across the Brazil-Malvinas Confluence, Journal of Geophysical Research: Oceans, 122, 3329-3357,
- 679 https://doi.org/10.1002/2016JC012611, 2017.
- 680 Müller, V. and Melnichenko, O.: Meridional Eddy Heat Transport Variability in the Surface Mixed Layer of the Atlantic
- 681 Ocean, Journal of Geophysical Research: Oceans, 126, e2021JC017 789, https://doi.org/10.1029/2021JC017789, 2021.
- 682 NASA: Sea-viewing Wide Field-of-view Sensor (SeaWiFS) level-2 ocean color data,
- 683 https://doi.org/10.5067/ORBVIEW-2/SEAWIFS/L2/OC/2018, NASA Ocean Biology Processing Group distributed active
- 684 archive center, 2018.
- 685 NOAA, National Oceanic and Atmospheric Administration, Physical Sciences Laboratory (PSL). Climate Indices: Monthly
- 686 Atmospheric and Ocean Time-Series. Available online: https://psl.noaa.gov/data/climateindices/list/ (accessed on 15 May
- 687 2024).
- 688 Nobre, P., Lemos, A. T., Giarolla, E., Camayo, R., Namikawa, L., Kampel, M., Rudorff, N., Bezerra, D. X., Lorenzzetti, J.,
- 689 and Gomes, J.: The 2019 northeast Brazil oil spill: scenarios, Anais da Academia Brasileira de Ciências, 94, e20210 391,
- 690 https://doi.org/10.1590/0001- 3765202220210391, 2022.
- 691 Oliveira, L. R., Piola, A. R., Mata, M. M., and Soares, I. D.: Brazil Current surface circulation and energetics observed from
- 692 drifting buoys, Journal of Geophysical Research: Oceans, 114, 10 006, https://doi.org/10.1029/2008JC004900, 2009.





- 693 Palma, E. D., Matano, R. P., and Piola, A. R.: A numerical study of the Southwestern Atlantic Shelf circulation: Barotropic
- 694 response to tidal and wind forcing, Journal of Geophysical Research: Oceans, 109, 8014,
- 695 https://doi.org/10.1029/2004JC002315, 2004.
- 696 Palma, E. D., Matano, R. P., and Piola, A. R.: A numerical study of the Southwestern Atlantic Shelf circulation: Stratified
- 697 ocean response to local and offshore forcing, Journal of Geophysical Research: Oceans, 113, 11 010,
- 698 https://doi.org/10.1029/2007JC004720, 2008.
- 699 Peterson, R. G.: The boundary currents in the western Argentine Basin, Deep Sea Research Part A. Oceanographic Research
- 700 Papers, 39, 623–644, https://doi.org/https://doi.org/10.1016/0198-0149(92)90092-8, 1992.
- 701 Pezzi, L. P., Quadro, M. F., Lorenzzetti, J. A., Miller, A. J., Rosa, E. B., Lima, L. N., and Sutil, U. A.: The effect of Oceanic
- 702 South Atlantic Convergence Zone episodes on regional SST anomalies: the roles of heat fluxes and upper-ocean dynamics,
- 703 Climate Dynamics, 59, 2041–2065, https://doi.org/10.1007/S00382-022-06195-3/TABLES/1, 2022.
- 704 Pilo, G. S., Mata, M. M., and Azevedo, J. L.: Eddy surface properties and propagation at Southern Hemisphere western
- 705 boundary current systems, Ocean Science, 11, 629–641, https://doi.org/10.5194/OS-11-629-2015, 2015.
- 706 Piola, A. R., Matano, R. P., Palma, E. D., Möller, O. O., and Campos, E. J. D.: The influence of the Plata River discharge on
- 707 the western South Atlantic shelf, Geophysical Research Letters, 32, 1–4, https://doi.org/10.1029/2004GL021638, 2005.
- 708 Poli, L., Artana, C., and Provost, C.: Topographically trapped waves around South America with periods between 40
- 709 and 130 days in a global ocean reanalysis. Journal of Geophysical Research: Oceans, 127, e2021JC018067, https://doi.
- 710 org/10.1029/2021JC018067, 2022.
- 711 Reichl, B. G. and Hallberg, R.: A simplified energetics based planetary boundary layer (ePBL) approach for ocean climate
- 712 simulations., Ocean Modelling, 132, 112–129, https://doi.org/10.1016/j.ocemod.2018.10.004, 2018.
- 713 Reagan, James R., Boyer, Tim P., García, Hernán E., Locarnini, Ricardo A., Baranova, Olga K., Bouchard, Courtney, Cross,
- 714 Scott L., Mishonov, Alexey V., Paver, Christopher R., Seidov, Dan, Wang, Zhankun, Dukhovskoy, Dmitry (2023). World
- 715 Ocean Atlas 2023. Salinity and Temperature. NOAA National Centers for Environmental Information. Dataset.
- 716 https://doi.org/10.25921/va26-hv25. Accessed October 2025.
- 717 Risaro D. B., Chidichimo M. P., Piola A. R.: Interannual Variability and Trends of Sea Surface Temperature Around
- 718 Southern South America, Frontiers in Marine Science, 9, https://www.frontiersin.org/articles/10.3389/fmars.2022.829144,
- **719** 2022.
- 720 Rocha, C. B., Silveira, I. C. D., Castro, B. M., and Lima, J. A. M.: Vertical structure, energetics, and dynamics of the Brazil
- 721 Current System at 22°S–28°S, Journal of Geophysical Research: Oceans, 119, 52–69,
- 722 https://doi.org/10.1002/2013JC009143, 2014.
- 723 Rodrigues, R. R., Taschetto, A. S., sen Gupta, A., & Foltz, G. R.: Common cause for severe droughts in South America and
- 724 marine heatwaves in the South Atlantic. Nature Geoscience, 12, 620–626. https://doi.org/10.1038/s41561-019-0393-8,
- **725** 2019.





- 726 Ross, A. C., Stock, C. A., Adcroft, A., Curchitser, E., Hallberg, R., Harrison, M. J., Hedstrom, K., Zadeh, N., Alexander, M.,
- Chen, W., Drenkard, E. J., du Pontavice, H., Dussin, R., Gomez, F., John, J. G., Kang, D., Lavoie, D., Resplandy, L.,
- Roobaert, A., Saba, V., Shin, S.I., Siedlecki, S., and Simkins, J.: A high-resolution physical-biogeochemical model for 728
- marine resource applications in the Northwest Atlantic (MOM6-COBALT-NWA12 v1.0), Geoscientific Model 729
- Development Discussions, 2023, 1–65, https://doi.org/10.5194/gmd-2023-99, 2023. 730
- 731 Schiller, A. and Ridgway, K. R.: Seasonal mixed-layer dynamics in an eddy-resolving ocean circulation model, Journal of
- Geophysical Research: Oceans, 118, 3387–3405, https://doi.org/10.1002/JGRC.20250, 2013.
- 733 Servain, J., Busalacchi, A., McPhaden, M., Moura, A., Reverfdin, G., Vianna, M., and Zebiak, S.: A pilot research moored
- 734 array in the tropical Atlantic (PIRATA), Bulletin of The American Meteorological Society, 79, 2019-2032,
- https://doi.org/10.1175/1520-0477(1998)079<2019:APRMAI>2.0.CO;2, 1998. 735
- 736 Stock, C. A., Pegion, K., Vecchi, G. A., Alexander, M. A., Tommasi, D., Bond, N. A., Fratantoni, P. S., Gudgel, R. G.,
- Kristiansen, T., O'Brien, T. D., Xue, Y., and Yang, X.: Seasonal sea surface temperature anomaly prediction for coastal 737
- ecosystems, Progress in Oceanography, 137, 219–236, https://doi.org/10.1016/j.pocean.2015.06.007, 2015. 738
- 739 Valerio, A. M., Kampel, M., Ward, N. D., Sawakuchi, H. O., Cunha, A. C., and Richey, J. E.: CO2 partial pressure and fluxes
- in the Amazon River plume using in situ and remote sensing data, Continental Shelf Research, 215, 104 348, 740
- https://doi.org/10.1016/J.CSR.2021.104348, 2021.
- 742 Wright, D. G.: An Equation of State for Use in Ocean Models: Eckart's Formula Revisited, Journal of Atmospheric and
- Technology, 740, 743 14,
- https://doi.org/https://doi.org/10.1175/1520-0426(1997)014<0735:AEOSFU>2.0.CO;2, 1997. 744
- 745 Wunsch, C. and Ferrari, R.: VERTICAL MIXING, ENERGY, AND THE GENERAL CIRCULATION OF THE OCEANS,
- 746 https://doi.org/10.1146/annurev.fluid.36.050802.122121,
- 36, 281-314,
- https://doi.org/10.1146/ANNUREV.FLUID.36.050802.122121, 2004.
- 748 Zsoter, E., Harrigan, S., Barnard, C., Wetterhall, F., Ferrario, I., Mazzetti, C., Alfieri, L., and Salamon, P.and Prudhomme, C.:
- discharge related historical data from the Global Flood Awareness 749 and System.
- 750 https://doi.org/10.24381/cds.a4fdd6b9, accessed 03 November 2023, 2021.
- 751 Zweng, M., Reagan, J., Seidov, D., Boyer, T., Locarnini, R., Garcia, H., Mishonov, A., Baranova, O., Paver, C., and Smolyar,
- I.: World Ocean Atlas 2018 Volume 2: Salinity, 2019.